Competition between baroclinic instability and Ekman transport under varying buoyancy forcings in upwelling systems: An idealized analog to the Southern Ocean

Soeren Thomsen, Xavier Capet, Vincent Echevin

Competition between baroclinic instability and Ekman transport under varying buoyancy forcings in upwelling systems: An idealized analog to the Southern Ocean.

Soeren Thomsen*, Xavier Capet, Vincent Echevin

LOCEAN-IPSL, IRD/CNRS/Sorbonne Universités (UPMC)/MNHN, UMR 7159, Paris, France

*Corresponding author: Soeren Thomsen, soeren.thomsen@locean.ipsl.fr

ABSTRACT

Coastal upwelling rates are classically determined by the intensity of the upper-ocean offshore Ekman transport. But (sub-)mesoscale turbulence modulates offshore transport, hence the net upwelling rate. Eddy effects generally oppose the Ekman circulation, resulting in so-called "eddy cancellation", a process well studied in the Southern Ocean. Here we investigate how air-sea heat/buoyancy fluxes modulate eddy cancellation in an idealized upwelling model. We run CROCO simulations with constant winds but varying heat fluxes with and without submesoscale-rich turbulence. Eddy cancellation is consistently evaluated with three different methods that all account for the quasi-isopycnal nature of ocean circulation away from the surface. For zero heat fluxes the release of available potential energy by baroclinic instabilities is strongest and leads, near the coast, to nearly full cancellation of the Ekman cross-shore circulation by eddy effects, *i.e.*, zero net mean upwelling flow. With increasing heat fluxes eddy cancellation is reduced and the transverse flow progressively approaches the classical Ekman circulation. Sensitivity of the eddy circulation to synoptic changes in air-sea heat fluxes is felt down to 125 m depth despite short experiments of tens of days. Mesoscale dynamics dominate the cancellation effect in our simulations which might also hold for the real ocean as the relevant processes act below the surface boundary layer. Although the idealized setting overemphasis the role of eddies and thus studies with more realistic settings should follow, our findings have important implications for the overall understanding of upwelling system dynamics.

1. Introduction

Along eastern boundary upwelling systems (EBUS) equatorward winds are responsible for a thermally indirect Ekman circulation that brings heavy, deep, and generally nutrient rich water towards the surface. Nutrient enrichment and new primary production have traditionally been thought to linearly depend on the intensity of the alongshore wind stress component (Bakun et al. 2010). This is what hundreds of studies concerned with EBUS ecosystem functioning have implicitly assumed by relying on the so-called Bakun index (derived from alongshore coastal winds, sometimes complemented by windstress curl information (i.e. the CUTI index by Jacox et al. (2018)), as a proxy for planktonic food availability. However, the rate at which water is being transferred from the ocean interior into the mixed layer may not be simply related to the Ekman transport.

Quite recently, the contribution of alongshore pressure gradients have increasingly been accounted for. In many upwelling sectors they can yield onshore velocities that counteract, or more infrequently reinforce, the Ekman flow (Colas et al. 2008; Marchesiello et al. 2010; Ndoye et al. 2017; Jacox et al. 2018). In this study, we shed light on another potentially important effect: quasi-balanced meso- and submesoscale turbulence is responsible for rectified eddy transport which also tends to counteract the Ekman upwelling cell. Several studies have addressed this topic (e.g. Lathuilière et al. 2010; Gruber et al. 2011; Colas et al. 2013) but the knowledge of the eddies role in EBUS remains fragmented. In an attempt to remedy this the present study borrows more directly from and draw connections with the Southern Ocean (SO) literature, in which eddy effects have been more extensively investigated (Marshall and Radko 2003; Hallberg and Gnanadesikan 2006; Morrison et al. 2011). In the SO, transport in the direction transverse to the Antarctic Circumpolar Current (ACC) axis computed in isopycnal coordinates is a small residual between

the mean Ekman-driven circulation due to wind pumping/suction (the so-called Deacon cell) and eddy-induced transfers of mass driven by baroclinic instability processes (Marshall and Radko 2006; Marshall and Speer 2012). The eddy-induced circulation attempts to flatten isopycnal surfaces, reduce available potential energy, and therefore largely opposes the thermally direct Deacon cell. As a result, it is widely accepted that the sole knowledge of the wind forcing does not provide useful insight into the mean cross-frontal circulation of the SO. There air-sea buoyancy fluxes are, somewhat counter-intuitively, much more informative than the wind forcing with respect to the meridional tracer transport (Marshall 1997; Gent 2016).

Indeed, they constrain rates of fluid transfer across isopycnals in the mixed layer, hence also subduction and obduction rates at the base of the mixed layer in steady state (subduction - resp. obduction - being related to a convergence - resp. divergence - of diapycnal flux of fluid, Fig. 1). Neglecting mixing in the ocean interior the time-averaged residual meridional transport is thus entirely determined by the knowledge of air-sea buoyancy fluxes (Walin 1982; Marshall 1997). In particular, with zero air-sea buoyancy fluxes the residual circulation in the surface layer (and in the interior) must vanish, which means that eddies exactly cancel the Eulerian wind-driven circulation (Fig. 1c).

The transverse across-shore circulation found in upwelling systems is often represented as a 2D cell as in Fig. 1a. Under the constraint of no divergence, fluid is being upwelled near the coast to feed the offshore Ekman drift induced by alongshore wind stress. Naively considered as a representation of a 2D, time averaged (or steady), and laminar (no eddy terms) upwelling, Fig. 1a poses a conundrum that we find a useful starting point. Consider the fluid transported by the Ekman circulation in the mixed layer. The thermohaline structure being steady this fluid crosses isopycnals as it moves offshore and a net buoyancy gain is needed that must exactly satisfy the relation:

$$v_{ek} \cdot \partial_y < \overline{b} >_{ml} (y) = \overline{B}_{ml}(y) \quad (1)$$

where v_{ek} is the wind-driven Ekman velocity vertically averaged over the mixed layer, $< \overline{b} >_{ml}$ is the mean buoyancy in the mixed layer, where $b = -g\rho/\rho_0$ with g being the gravitational acceleration, ρ the potential density, and ρ_0 a reference density. $\overline{B}_{ml}$ is the net buoyancy supply to the mixed layer, supposed to mainly result from air-sea exchanges sector where coastal upwelling is taking place (Fig. 2). The derivation of Eq. (1) is detailed in Appendix 1.

By analogy with the SO, we hypothesize and will demonstrate that: (i) in a 3D upwelling system eddy fluxes are responsible for a large contribution to the time and/or alongshore average buoyancy equation (ignored in Eq. (1), see Eq. (A3)) that cancels a fraction of the buoyancy advection by the Eulerian Ekman circulation (ii) the structure and intensity of the eddy and residual circulation is modulated by the buoyancy input $\overline{B}_{ml}(y)$. (i) is a key finding in a few past studies (Gruber et al. 2011; Colas et al. 2012, 2013; Nagai et al. 2015), which is also true for tracers other than buoyancy (Lathuilière et al. 2010; Gruber et al. 2011) and will subjected to careful considerations herein. (ii) is an original result of this study which is demonstrated by analysing the synoptic response of upwelling dynamics to buoyancy fluctuations.

One practical difficulty is that upwelling systems lack the periodicity attribute so the ACC framework and theory are not directly applicable. Net buoyancy input can arise from lateral fluxes at the northern and southern edges of the upwelling region and this is an important source of complication. In addition most upwelling systems have intense seasonal fluctuations, so time averaging over one or several years and widely distinct ocean states is needed to ensure that the neglect of the buoyancy tendency term in Eq. (1) is valid (see Appendix).

To make progress in the overall understanding of EBUS functioning, we thus consider an idealised upwelling configuration with periodic boundary conditions following Lathuilière et al. (2010). The

setting and methods are described in section 2. How these results can be interpreted in the context of real ocean upwelling systems is extensively discussed in section 4. The paper finishes with our conclusions in section 5.

2. Model setup and methods

a. Idealized upwelling model configuration

The ocean circulation model CROCO (Coastal and Regional Ocean COmmunity model, www.croco-ocean.org) is used in an idealized upwelling configuration. CROCO is formulated in terrain-following sigma coordinates. The size of the computational domain is 400 km (L_x) by 600 km (L_y) long in the alongshore (x) and cross-shore (y) direction respectively (Fig. 3). The bottom topography h(x,y) consists of a narrow shelf, a continental slope and a flat bottom over the open ocean (Figs. 3). h(x,y) is defined by the following analytic function:

$$h_i(x,y) = h_{max}\left[\frac{1}{2}\left(1+tanh\left(\frac{y-y_s}{L_s}\right)\right)\right]+\delta h_i(x) \tag{2}$$

with h_{max} = 1960 m, y_s = 100 km, L_s = 50 km. With these parameter values for Eq. (2) the minimum depth at y = 0 km is 34 m and the shelf is about 50 km wide (Fig. 5c). Note that the bottom topography is uniform in the alongshore direction except for a small perturbation $\delta h_i(x)$ with i being the index of the i^{th} ensemble run (see details in section 2b).

We use periodic boundary conditions in the alongshore direction. At the coastline the domain is closed. For numerical simplicity a closed boundary is also present along the offshore side of the domain. To limit the spurious effects of this western wall a sponge layer of width equal to 96 km is included in which momentum and temperature are subjected to harmonic diffusion and temperature is restored toward a background temperature profile $T_o(z)$ (see Eq. (3)). In all simulations diffusion and viscosity coefficients increase smoothly via a cosine function from 0

m^2/s at y = 506 km to a maximum value of 600 m^2/s towards the closed boundary at y = 600 km (Fig. 3). For lateral momentum advection the default CROCO 3rd-order upstream biased advection scheme with implicit diffusion is used. For temperature we use a 5th-order WENOZ quasi-monotonic advection scheme to prevent temperature under/overshoots near sharp horizontal fronts.[1] Spurious diapycnal mixing associated with this scheme cannot be entirely avoided but shall have negligible effects in our study because 1) sigma-coordinates are quasi-horizontal over most of the domain where the bottom is flat, 2) we are concerned with the upper 100-150 m of the water column in which (physical) diapycnal mixing rates are moderately high 3) we use kilometre scale horizontal resolution (except for some sensitivity runs; see Marchesiello et al. (2009) and Lemarié et al. (2012) for relevant details on spurious diapycnal mixing). Free slip boundary conditions are used at the onshore and offshore walls. Linear friction with a drag coefficient $d_{bottom} = 6 * 10^{-4}$ m/s is applied at the ocean bottom.

The temperature profile $T_o(z)$ is also used as an homogeneous initial condition for all simulations. It is chosen to be typical of (sub)tropical EBUS. Specifically we choose the mean climatological temperature profile of the CARS 2009 database (www.cmar.csiro.au/cars, Ridgway et al. (2002); Condie and R. Dunn (2006)) for the month of January at 15°S / 86°W off Peru. For simplicity and easier reproducibility we fit this profile with the following analytic function:

$$T_0(z_k) = T_a \left[1 + h_1 \, log \left(cosh\left(\frac{z_k - h_2}{h_1} \right) / cosh\left(\frac{z_{k-1} - h_2}{h_1} \right) \right) / (z_k - z_{k-1}) \right] + T_b * exp(\frac{z_k}{1000}) \tag{3}$$

with the following constants: $T_a = 4°C$, $T_b = 15.5°C$, $h_1 = 80\,m$ being the vertical scale of the thermocline width, $h_2 = -80\,m$ being the depth of the thermocline center and k the index of the vertical grid coordinate with $z(k = 1) = 1960$ and $z(k = 100) = 0\,m$. The first part of Eq.

[1] $https://croco-ocean.gitlabpages.inria.fr/croco_doc/model/model.numerics.overview.html$

(3) prescribes the intensified stratification within the upper 250 m as typically found in eastern boundary systems. The second part can be interpreted as a weakly stratified main thermocline present over the full water column (Fig. 3).

The Coriolis parameter ($f = -2\pi/T_f$) is set constant (no β effect) and corresponds to a f-plane latitude of about 14.5°S resulting in an inertial period (T_f) of 2 days. Due to the absence of any β effect, there is no westward propagation of Rossby waves. This is not of major importance as we restrict the duration of our experiment to 120 days (including a spinup of 80 days) but is presumably responsible for eddy kinetic energy (EKE) levels above typical values found in the real ocean for EBUS sectors (Haney et al. 2001; Marchesiello et al. 2003; Gruber et al. 2011). The first baroclinic Rossby Radius is around 57 km within our idealized setting. This choice of parameters makes our results applicable to the Peruvian, West African and northern Benguelan upwelling systems but the main findings should also be valid at higher latitude.

In order to resolve sharp vertical velocity and temperature gradients in the upper ocean, we use 100 vertical sigma levels for all configurations. The vertical coordinate by Shchepetkin and McWilliams (2009) are used with the vertical grid parameters $theta_s = 6$, $theta_b = 0$ and hc = 10. Upwelling systems typically have water depth between 4000 m and 6000 m offshore of the continental slope. Here we use a reduced bottom depth of 1960 m in combination with the high number of vertical levels results in a relatively high vertical resolution especially near the surface. Over the upper shelf the vertical resolution ranges from 0.1 m near the surface to 1.2 m above the bottom. Offshore the vertical resolution ranges from 0.7 m at the surface to 6 m at 100 m depth and 112 m near the bottom.

In our reentrant upwelling channel no along-shore pressure gradient can a priori exist at the system scale due to the periodic boundary conditions. Without an along-shore pressure gradient no interior geostrophic onshore flow can be established. Feeding the surface Ekman flow would

therefore involve bottom Ekman transport, thereby limiting the realism of the model for most upwelling sectors (Lentz and Chapman 2004). Following Lathuilière et al. (2010) we alleviate this difficulty by adding a constant and horizontally homogeneous alongshore pressure gradient to the momentum equation driving an onshore return flow V_{PG}:

$$V_{PG}(z) = \frac{-\tau_x}{f(H_{PG} - H_{Ekman})} \qquad \text{if} - H_{PG} < z - < H_{Ekman}, \text{and zero otherwise.} \tag{4}$$

with H_{Ekman} = 45 m and H_{PG} = 200 m. All simulations are spun up from the initial resting state $T(y,z) = T_0(z)$, where T_0 is defined in Eq. (3). The alongshore wind forcing (τ_x) increases slowly with a ramp from 0 to the maximum value of 0.075 Nm^{-2} over a time period of t = 4 days:

$$\tau_x(t) = 0.075 \left[sin\left(\frac{\pi t}{8}\right) + 0.075\, cos\left(\frac{\pi t}{8}\right)\right] \tag{5}$$

After day 4 all runs are forced with constant wind stress forcing of 0.075 N/m^2 (Fig. 4a).

b. Heat flux sensitivity experiments and ensemble runs

An important aim of this study is to investigate the effects of varying atmospheric buoyancy (here heat) forcing on upwelling dynamics and more specifically buoyancy advection. A simple heat flux formulation is chosen based on restoring to a reference SST which equals $T_0(0)$ to be consistent with the initial conditions and the restoring at the offshore edge of the domain. The heat flux into the ocean is thus given by the following formula:

$$Q(x,y,t)_{heat} = \frac{1}{\rho_0 Cp} \cdot \frac{dQ}{dT}(SST_m(x,y,t) - T_0(0)) \tag{6}$$

with dQ/dT being the relaxation coefficient in W K^{-1}, and SST_m the model SST (Barnier et al. 1995). ρ_0 corresponds to the reference density (1025 kgm^{-3}) and Cp is the heat capacity of seawater (3985 $Jkg^{-1}K^{-1}$). During the spin up period until day 80 the relaxation coefficient dQ/dT is kept constant at -25 $Wm^{-2}K^{-1}$ (Fig. 4b). To modulate heat fluxes we artificially modify dQ/dT.

After day 80 dQ/dT is adjusted so as to conduct three sensitivity runs: (i) no heat flux (dQ/dT = 0, hereafter NF), (ii) moderate heat fluxes (dQ/dT remains equal to -25 $Wm^{-2}K^{-1}$, MF) and (iii) enhanced heat fluxes (dQ/dT = -50 $Wm^{-2}K^{-1}$, HF). MF experiments receive on average a heat input of about 200 Wm^{-2} near the coast and 50 Wm^{-2} 200 km offshore (Fig. 5a). These values are typical of net heat flux forcings in EBUS although large variability exists (Fig. 2).

Heat flux sensitivity experiments are carried out at meso- (Δx = 8 km) and submesoscale permitting (Δx = 800 m) resolution. Additional information about the simulation settings is given in table 1. Due to the turbulent nature of the ocean the eddy fluxes are not solely determined by the forcings and are subjected to intrinsic stochastic variability (in addition to not being in statistical equilibrium). The duration of each experiment is only 40 days, which is insufficient to get statistically reliable averages. Thus we perform 12 ensemble runs for each experiment listed in table 1. Ensemble runs differ from each other by small-amplitude perturbations $\delta h_i(x)$ added to the alongshore invariant bathymetry, which are responsible for triggering instabilities of the upwelling flow. Specifically, we use:

$$\delta h_i(x) = -\frac{1}{2} sin(2\pi m_i \frac{x}{L_x}) - \frac{1}{2} sin(2\pi n_i \frac{x}{L_x}) \tag{7}$$

with 12 factor pairs (m_i, n_i) being (4,7), (2,9), (6,5), (3,2), (5,2), (2,1), (1,4), (1,6), (1,8), (4,9), (4,5), (4,3).

c. Quantification of eddy effects and overturning streamfunction calculation

Our periodic upwelling channel is oriented in the alongshore (x) direction. Within the whole study we define the perturbation of a variable X as the deviation from the alongshore average ($\overline{X}^x$):

$$X'(x,y,z,t) = X(x,y,z,t) - \overline{X}^x(y,z,t). \tag{8}$$

Temporal averaging (denoted $\overline{X}^{t}$) is also frequently performed over the time window from day 81 to day 120 that excludes spin up. Averaging over all realizations of a given ensemble run is denoted $\overline{X}^{e}$. $\overline{X}^{x,t,e}$ is abbreviated as $\overline{X}$.

Baroclinic instability (hereafter BCI) processes are known to be essential in upwelling systems as a source of meso- and submesoscale turbulence (Marchesiello et al. 2003). The strength of BCI will be classically evaluated by computing available potential energy (APE) release as the averaged covariance of the vertical velocity (w) and buoyancy (b) perturbations: $\overline{w'b'}$. Buoyancy is defined here as a function of temperature with $b = -g\alpha T/\rho_0$ with $\alpha = 0.24\, kg°C/m^3$, $g = 9.81\, m/s^2$.

Our focus is on the description of the eddy role on the transport of buoyancy. In practice, we will use three different approaches to determine variants of residual overturning (transverse) streamfunctions: 1) the transformed Eulerian mean formulation of Held and Schneider (1999); isopycnal averaging of water volume flux at 2) constant across-shore distance (equivalent to averaging at constant latitude in the SO, Döös and Webb 1994); or at 3) constant depth (Nurser and Lee 2004a,b). Each of these three approaches has its own advantages and limitations as detailed below. Thus we apply all three of them to ensure that our main findings are robust, as previously done for the SO or in the atmosphere.

The first formulation explicitly involves the rate of APE release and is able to accommodate outcropping situations. Following Held and Schneider (1999) (see also Colas et al. 2013) we define an eddy streamfunction for the transformed Eulerian mean circulation as $\Psi^{TEM}_{Eddy}(y,z) = \overline{w'b'}/\overline{b_y}$ where $\overline{b_y}$ is the mean cross-shore buoyancy gradient. Being computed at fixed location Ψ^{TEM}_{Eddy} can be easily compared to the Eulerian mean streamfunction

$$\Psi_{Mean}(y,z) = \overline{\int_z^0 v(x,y,z,t)}^{x,t,e} \quad dz \tag{9}$$

Simple Eulerian averaging is well known to produce transport fields with unrealistically large diapycnal components (i.e. the flow associated with Ψ_{Mean} crosses the mean isopycnal surfaces and is therefore inconsistent with the weakly diabatic nature of interior ocean circulation). $\Psi_{Res}^{TEM} = \Psi_{Mean} + \Psi_{Eddy}^{TEM}$ is one estimation of the residual circulation advecting mean buoyancy and accounting for eddy effects.

A more natural way to account for the quasi-adiabatic nature of oceanic motions is to perform averages using moving density surfaces (or here equivalently temperature surfaces) as vertical reference levels. To this end, we define the second formulation:

$$\Psi_{Res}^{iso-h}(y, T_0) = \overline{\int \int_{(x,z,t):T(x,y,z,t) \leqslant T_0} v(x, y, z, t)\, dx\, dz}^{t,e} \tag{10}$$

Heaving of the isopycnals (here also isotherms) by eddies is absorbed into Ψ_{Res}^{iso-h} which thus includes an eddy contribution. Ψ_{Res}^{iso-h} can be remapped back into depth space using the mean height of each isotherm as a function of cross-shore distance $\overline{z(T, y)}^{x,t,e}$ (see Nurser and Lee (2004a) section 2c). Doing so, an eddy contribution to Ψ_{Res}^{iso-h} can be defined as:

$$\Psi_{Eddy}^{iso-h}(y, z) = \Psi_{Res}^{iso-h}(y, z) - \Psi_{Mean}(y, z) \tag{11}$$

Near the surface, averaging and integration using temperature as a vertical coordinate poses some issues. Specifically, the remapping from temperature to depth space becomes problematic wherever the water column becomes well-mixed or nearly so. In addition, rare occurrences of warm water conditions at the surface strongly imprint on the form of Ψ_{Res}^{iso-h} and its remapping (Nurser and Lee 2004a). To remedy this, an alternative quasi-lagrangian approach, the third formulation here, involves isopycnal averaging at constant height but variable cross-shore distance (or latitude in the ACC context):

$$\Psi_{Res}^{iso-v}(T_0, z) = \overline{\int \int_{(x,y,t):T(x,y,z,t) \leqslant T_0} w(x, y, z, t)\, dx\, dy}^{t,e} \quad . \tag{12}$$

Ψ_{Res}^{iso-v} corresponds to the vertical transport of fluid colder than a temperature T at any given depth z. The proximity to the ocean surface has no effect on this method. On the other hand, isothermal averaging at constant z is strongly impacted near side boundaries where the structure of Ψ_{Res}^{iso-v} can be difficult to interpret (Nurser and Lee 2004a; Lee and Nurser 2012). See section 2c in Nurser and Lee (2004a) for more details.

The ocean sector where upwelling takes place is in close proximity to the eastern boundary and not situated very deep below the surface. Indeed we are typically interested in the depth range from below the mixed layer down to 150-200 m depth or less, i.e., the source region of the upwelled water. The interpretation of the transport streamfunctions Ψ_{Res}^{iso-h} and Ψ_{Res}^{iso-v} is thus subject to caution. Below we present and compare all approaches. The degree of resemblance between Ψ_{Eddy}^{TEM}, Ψ_{Eddy}^{iso-h} and Ψ_{Eddy}^{iso-v} will be considered as an indication of robustness.

3. Results

a. General hydrography and circulation in the idealized upwelling system

The general thermal structures and circulation features of the idealised upwelling configuration resemble those typical of real upwelling systems (Figs. 5, 6). The wind forcing results in an offshore Ekman transport in the upper 30 - 40 m of the water column (Fig. 5d). The Ekman cell (Ψ_{Mean}) is closed by a return flow reaching down to 200 m depth and has a maximum strength of 2.3 $m^2 s^{-1}$ around 50 m depth (Fig. 5d). The Eulerian circulation is broadly consistent with isopycnal doming in the upper 150 m of the water column especially within 80 km from shore (Figs. 5c,d). Mean surface temperatures as low as 14 $^{\circ}C$ are simulated at the shelf break (Figs. 5c,d). A frontal zone separates the upwelling waters from the open ocean where surface temperatures increase to 20 $^{\circ}C$ at 200 km offshore (Figs. 5c, d). An alongshore surface jet of about 0.4 ms^{-1}

in same direction as wind forcing develops over the shelf and upper slope (Fig. 5c). A subsurface undercurrent in opposite direction hugs the continental slope with maximal velocities of $0.15\,ms^{-1}$ in $150-200\,m$ depth (Fig. 5c).

The idealized upwelling solution also produces turbulent structures as found in upwelling systems: mesoscale eddies, filaments and sharp submesoscale temperature fronts particularly at the finest resolution (Fig. 6a). Typically an anticyclonic mesoscale warm core eddy forms at some point near the shelf break with diameter of roughly 150 km and a sea level anomaly of about 10 cm (Figs. 6a, b). Several smaller scale cyclonic vortices are formed around the anticyclone with cold filaments at the edges of the mesoscale structures (Figs. 6a, b). Within the filaments the SST can drop down to about $18°C$. Submesoscale frontal dynamics are obviously richer at the higher resolution. Downwards velocities of up to 100 m/day are found at the cold side of these fronts (e.g. at x = 150 - 200 km and y = 150 km in Fig. 6c). These vertical velocities are a crucial part of the eddy flow that counteracts the Ekman transport of buoyancy as we investigate in detail in the following chapter through three different approaches.

b. Eddy effects under varying heat flux forcing

The effect of varying heat flux forcing on the cross-shore circulation is investigated in this section. Based on the SO literature our hypothesis is that changing heat fluxes affects the eddy field with implications on the eddy heat fluxes, hence also on the eddy-induced and residual transverse circulations. To test this, we compute the 3 different variants of eddy and residual streamfunctions defined in section 2c. This is done for the submesoscale permitting simulations which represent the turbulent processes more accurately. A detailed comparison between the simulations with 8 km and 800 m horizontal resolution is carried out in the next section 3c.

We first quantify the APE release by BCI to start looking into the eddy effect sensitivity to heat fluxes. The mean cross-shore distribution of $\overline{w'b'}$ shows maximum values above $1.8 \cdot 10^{-7} m^2 s^{-3}$ at 20 m depth at around 30 km offshore during the NF case at submesoscale resolution (Fig. 7a). Further offshore 200 km from the coast the maximum values decrease to values from 0.6-$0.9 \cdot 10^{-7} m^2 s^{-3}$ in 20 m depth (Fig. 7a). With increasing air-sea flux $\overline{w'b'}$ decreases (Fig. 7c) from maximum values $1.44 \cdot 10^{-7} m^2 s^{-3}$ in the NF case to $1.06 \cdot 10^{-7} m^2 s^{-3}$ in the HF case, when averaged between 16 to 112 km offshore. This represents a decrease of about 25%. The shoaling of the maximum $\overline{w'b'}$ (19 m in NF and 15 m in HF, Fig. 7c) is associated with a thinning of the mixed layer (27 m in NF and 23 m in HF, Fig. 7c) with increasing air-sea flux. Although $\overline{w'b'}$ exhibits a marked decline with depth below the mixed layer, it remains enhanced down to about 100 m depth within about 100 km from the shore, *i.e.*, where the tilt of the isopycnals is most pronounced (Fig. 7a). The modulation of BCI strength by air-sea fluxes reaches down to similar depths (compare $\overline{w'b'}$ in Fig.7c; at 75 m depth $\overline{w'b'}$ is reduced by about 50% in the HF compared to NF). Below 125 m depth the domain-averaged $\overline{w'b'}$ curves for all air-sea flux cases show almost no difference and vanish at around 200 m depth (Fig. 7c), consistently with the relatively shallow extension of mesoscale turbulence in EBUS (Capet et al. 2008).

We now turn to the effects of turbulence on buoyancy advection and start with the most dramatic NF case. Ψ^{TEM}_{Eddy} is shown in Fig. 7b. Its sign is systematically negative and it almost mirrors the structure of the mean streamfunction (Ψ_{Mean}) shown in Fig. 8a. The eddy streamfunction reaches values down to -2.8 $m^2 s^{-1}$, which is stronger (in opposing direction) than the mean Eulerian streamfunction (2.3 $m^2 s^{-1}$, Fig. 5d). Note that this characteristic of overcancellation is absent or attenuated in Ψ^{iso-h}_{Eddy} and Ψ^{iso-v}_{Eddy} (Figs. 8e and 9e). The recirculation confined in the mixed layer revealed by Ψ^{TEM}_{Eddy} (and to a lesser extent Ψ^{iso-v}_{Eddy}) is the signature of submesoscale-driven mixed layer restratification (Fox-Kemper et al. 2008). As expected this signature is improperly captured

by isopycnal averaging at constant cross-shore distance (Held and Schneider 1999). It is the main point of disagreement between the three variants. In the ocean subsurface (at 50 - 100 m depth) where we seek to understand the eddy effect on buoyancy advection, all three formulations agree on patterns and intensity, even close to shore where the effect of the ocean boundary is supposed to impact differently on each of them (see section 2c).

Mean-Eddy cancellation is manifest in Figs. 8i and 9i. In the upper 50 m at 200 km and even down to 100 m closer to the shelf break the intensity of the residual circulation is smaller than that of the mean Eulerian circulation by a factor 4 or more. Most importantly, advective feeding of the surface layer with upwelling water vanishes. At greater depth (125 m) residual streamfunction values above 1 $m^2 s^{-1}$ are found away from the coast (Fig. 8i) where the tilt of the isopycnals and BCI strength (Fig. 7a) is reduced. Note that the residual circulation below the surface layer is not particularly better aligned with the isopycnals than the mean Eulerian circulation, contrary to what is typically found in the SO (Karsten and Marshall 2002). There are two reasons for this. First, our simulations are not in statistical equilibrium so that transient adjustments might be responsible for apparent "mean" diapycnal flow over the period of analysis. The fact that our simulations for the different air-sea flux cases exhibit similar residual circulations indicates that this reason is secondary. Second, and more importantly, our entire region of interest is in close proximity to the mean ML base and it is subjected to intense intermittent mixing. To substantiate this statement, we show the maximum mixed layer depths reached for every simulation in Fig. 7. More specifically, mixed layer depths between 60 and 100 m are reached in 5% of the time. Although our simulations do not resolve all relevant processes, a transition layer with relatively elevated mixing levels is found below the mixed layer (Large et al. 1994; Johnston and Rudnick 2009). This provides the required diabatic forcing to accommodate a slow but non-zero residual circulation consistent with upwelling to about 80 - 120 m depth which bifurcates offshore above this depth range (Figs. 8i,

9i). This circulation pattern is very similar for Ψ^{iso-v}_{Eddy} and Ψ^{iso-h}_{Eddy} which provides confidence in its robustness, despite the proximity of the ocean surface and coastline. By analogy with recent descriptions of the SO overturning circulation (Garabato et al. 2007; Silvester et al. 2014) one may see this feature as a short-circuiting of the coastal upwelling cell, resulting from the combination of eddy cancellation and mixing.

How these results are affected by the air-sea buoyancy forcings is described in the remainder of this section. In contrast to Ψ_{Mean}, the sensitivity of the eddy-induced and residual circulation to air-sea heat forcing is noticeable well below the mixed layer base (Figs. 9h, l). For instance, the lower part of the eddy cell weakens by over 50% (from -1.3 $m^2 s^{-1}$ in NF to -0.55 $m^2 s^{-1}$ in HF) at 70 km offshore and 75 m depth. Although a large degree of eddy-mean cancellation is still present at HF its residual circulation has recovered a structure that more closely resembles the mean Ekman circulation, with some streamlines unambiguously connecting the offshore-subsurface to the nearshore-surface sectors. Again no major difference is found between the sensitivities exhibited by Ψ^{iso-h}_{Res} and Ψ^{iso-v}_{Res} below the mixed layer (compare Figs. 8h,l and 9h,l). In the mixed layer, Ψ^{iso-v}_{Res} displays a reduction of the submesoscale restratification tendency consistent with theory, which confirms the superiority of this formulation near the ocean surface (Held and Schneider 1999).

Subtle differences between simulations with different heat fluxes are more readily apparent in Fig. 10 where streamfunction values are shown at a particular location chosen because it lies on the (Eulerian) mean upwelling pathway (see 'x' symbol in Figs. 8 and 9). Fig. 10 also gives a sense of the dispersion among realizations from the ensemble runs. The behaviors of Ψ^{TEM}_{Eddy} and Ψ^{iso-v}_{Eddy} as the heat flux forcing changes are very similar. The largest incoherence between formulations is found for NF with Ψ^{iso-h}_{Eddy} being $\sim 20\%$ larger than Ψ^{TEM}_{Eddy} and Ψ^{iso-v}_{Eddy}. At the chosen location, the eddies cancel between 72% (Ψ^{iso-v}_{Eddy}) and 87% (Ψ^{iso-h}_{Eddy}) of the Ekman transport for NF while the

cancellation reduces to between 46% (Ψ^{iso-v}_{Eddy}) and 60% (Ψ^{iso-h}_{Eddy}) for MF (Fig. 10b). In the HF case all 3 methods show cancellation levels of around 40 %. Beyond modest quantitative differences the main robust conclusion concerns the sensitivity of the eddy and residual circulation to air-sea heat fluxes: just as the Walin theory would predict in a steady state situation, mean buoyancy advection by the Ekman indirect overturning circulation is strongly counteracted by the eddies when the air-sea heat fluxes are such that no or limited diapycnal flow occurs in the surface layer. Pending discussion in section 4, note though that the elevated degree of cancellation we obtain is for an upwelling configuration in which EKE is well above typical EBUS values.

c. Resolution sensitivity

Submesoscale frontal processes are well known to be instrumental in the dynamics of the mixed layer. Our focus is on the dynamics in a layer of upper ocean fluid situated below the mixed layer, where the role of the submesoscale has not been clearly established and may vary depending on the regime under consideration (Capet et al. 2016). The influence of resolution on our findings is thus investigated, by comparing analyses for simulations at Δx = 800 m with analogues at Δx = 8 km.

Starting with $\overline{w'b'}$ is instructive. Inspecting Figs. 7a,c,d confirms that submesoscale processes (poorly represented in mesoscale runs) matter in the mixed layer and immediately below it. Below 50 m depth release of available potential energy in meso- and submesoscale runs are indistinguishable. Notably, in the present idealized EBUS regime, the factor ten difference in resolution does not dramatically alter the magnitude of $\overline{w'b'}$ in the mixed layer: for NF maximum values reach 1.44 (resp. 1.15) $m^2 s^{-3}$ at Δx = 800 m (resp. Δx = 8 km), which corresponds to a decrease of about 25%. Similar decreases are found between simulations with medium and high heat fluxes.[2]

[2]This result is seemingly at odds with previous studies including Colas et al. (2012; their figure 10) where a 15-fold increase in horizontal resolution strongly increases APE to EKE conversion near the surface. In reality, note that the absolute change in mixed-layer $\overline{w'b'}$ when going

The mean cross-shore buoyancy gradient $\overline{b}_y$ being weakly sensitive to resolution similar reductions of about 25% are found for the intensity of Ψ_{Eddy}^{TEM} in the mixed layer (compare Figs. 7b and e). Below the mixed layer eddy streamfunction differences between meso- and submesoscale simulations are small and presumably not significant given the dispersion within the ensemble runs. Also note that eddy and residual streamfunctions exhibit small spatial variations in their cross-shore-depth structures at different resolution, so the single point comparison in Fig. 10 should not be overinterpreted.

In short the eddy cancellation mechanism and its sensitivity to air-sea buoyancy forcing highlighted in the previous section for submesoscale-permitting simulations results mainly from mesoscale turbulence effects. Although this may seem surprising given the shallow nature of the problem under consideration this is consistent with the limited vertical extension of submesoscale turbulence, which is typically confined into the mixed layer in most oceanic regimes (see (Capet et al. 2016) for a counter-example where Charney instability is present).

4. Discussion

The overarching objective of this research is to contribute to the understanding of the factors influencing upper ocean enrichment in nutrients, primary production, and the fate of organic matter in EBUS, including considerations on their temporal variability and spatial heterogeneity (*e.g.*, differences between upwelling systems or upwelling sectors within a given EBUS). The results suggest that i) the eddy-induced circulation can counteract (or cancel in the SO terminology) mean advection by the Ekman circulation to a large degree ii) the level of cancellation can be subjected to spatio-temporal modulations due to air-sea buoyancy flux variability which can lead to changes

from mesoscale to submesoscale rich model resolution is quite similar in Colas et al. (2012) and our work ($2.8 \cdot 10^{-8}$ in our NF case in Fig. 7c versus $4.5 \cdot 10^{-8}$ for the winter season off Peru in Fig. 10 of Colas et al 2012). The reason why the comparison is misleading at first sight is the great difference in subsurface mesoscale $\overline{w'b'}$ between our idealized simulations and a real upwelling system like the Humboldt system (see section 4).

in the degree to which eddy fluxes counteract the mean advection by the Ekman flow that is central in coastal upwelling dynamics. This being said, the cancellation mechanism has been investigated in a simplified numerical configuration which has three important limitations in terms of realism.

First and foremost, the simulations we analyse have EKE levels that significantly exceed those found in the real ocean, by a factor 2 to 10 depending on which EBUS sector is considered. Elevated EKE is an inherent consequence of our periodic channel simplification with which the β-effect is not compatible. The absence of beta precludes the westward radiation of energy, for instance through Rossby wave propagation or beta-drift of vortices (Carton 2010). To make progress despite this important caveat we assume that the intensity of the eddy overturning streamfunctions scales linearly with EKE. Marshall et al. (2012) and Mak et al. (2017) provide some support to do so although obviously not in the specific context where the aim is to account for a missing β-drift. Fig. 11 is produced based on this assumption, on the EKE-degree of cancellation pairs obtained for each of our simulations, and on the EBUS EKE values reported by Gruber et al. (2011). See caption of Fig. 11 for more details. It provides estimates for the amount of cancellation in the four EBUS, going from 3 to 6% in the northern Benguela, to 10 to 30% in the California Current System. Upper range values correspond to situations with ≈ 0 net air-sea buoyancy fluxes which are not very common in this latter system when upwelling conditions prevail. These results are consistent with the well-accepted view that the role of eddies in EBUS is not of leading-order (as it is in the SO). But they point to the possible importance of eddy-induced circulations during periods when air-sea buoyancy forcings are weak and perhaps more so when they are temporarily negative (see Fig. 2). Note that this situation was not investigated. Eddy fluxes may also have an appreciable time-averaged effect on tracer advection in sectors of the California Current System where standing meanders yield intensified meso- and submesoscale activity (Centurioni et al. 2008; Colas et al. 2013). An important caveat regarding this rescaling approach concerns the possibly

subtle relationship between the cross-shore EKE distribution and the cancellation of the Ekman cell by eddies. Take for instance the southern Benguela where offshore Agulhas rings lead EKE levels in excess of 400 $m^2 s^{-2}$ just offshore of the continental shelf (Capet et al. 2008). Mesoscale structures produced remotely by the Agulhas retroflection or by the baroclinically unstable offshore flowing California Current contribute to EKE in the vicinity of the coastal upwelling sector. However these structures may not be an important local source of APE to EKE conversion, which is more naturally related to cancellation (see the formulation of Ψ^{TEM} above). Most generally, the local relationships between surface EKE, upper ocean $\overline{w'b'}$, and ultimately Ψ^{TEM}, involve various processes, including horizontal advection of EKE to which beta drift is a leading-order contributor (Chelton et al. 2011). Thus, cancellation estimates derived from Fig. 11 ignore, for instance, the fact that beta drift is more effective at low latitude which fundamentally alters the $\overline{w'b'} - EKE$ relationship. Regional ocean models can be very useful to make further progress (see below). Our study suggests that such model need not resolve submesoscale processes: eddy cancellation of the Ekman flow depends on subsurface turbulence which, our study demonstrates, remains overwhelmingly linked to the mesoscale despite the strong frontality of the environment under investigation.

Second, our study was based on numerical simulations that were analysed only over specific time periods of 40 days. Our findings on the cancellation process itself do not specifically depend on this particular time scale but the modulation of the cancellation in response to air-sea buoyancy fluctuations may. To explore this potential issue, we have computed the temporal evolution of the APE release rate $\overline{w'b'}^{x,e,S}(t)$ over the area S where the cancellation process is most important and defined by: $y_1 < y < y_2$ and $z_1 < z < z_2$ with y_1 = 16 km, y_2 = 112 km, z_1 = 0 m and z_2 = 80 m. Comparison between the $\overline{w'b'}^{x,e,S}(t)$ evolutions after day 80 for the three heat flux forcings reveals a fast adjustment process that takes place over about 3-5 days (not shown). This time scale may seem short for a BCI process that we have previously associated with the mesoscale. We are presently

unable to offer additional insight into this. Following this initial adjustement, APE release remains approximately stable until day 120 (not shown). From this we infer that the modulation of the eddy cancellation process in response to environmental changes should occur on synoptic and longer times scales (including seasonal and interannual) but not on shorter time scales, e.g., as a response to a diurnal cycle. In all EBUS air-sea buoyancy fluxes exhibit fluctuations of large magnitude on synoptic and seasonal time scales as illustrated in Fig. 2 for nearshore sites. Strong ocean cooling events (-200 to -500 W m^{-2}) can occasionally occur in 3 of the 4 EBUS. Additional experiments would be required to investigate the role of meso- and submesoscale processes in these relatively rare situations where mixed layer depth can reach 100 m, which complicates comparisons between cases. Net heat fluxes values are more typically in the range 0 - 150 W m^{-2} (Fig. 2b), *i.e.*, consistent with the forcings used in this study whose results should therefore be relevant to the real ocean, provided that the rescaling of cancellation based on EKE levels proposed above is correct.

Third, for simplicity, wind variability has been ignored throughout the study whereas it is an important aspect of upwelling dynamics. In the real ocean wind and air-sea buoyancy flux variability may be correlated and combine to produce results distinct from those found in this study. Such correlations vary from place to place (Send et al. 1987; Beardsley et al. 1998; Flynn et al. 2017; Lübbecke et al. 2019). For instance low winds can yield large (resp. weak) air-sea net heating into the surface ocean because cooling through latent heat release is reduced (resp. because in some regions like central California upwelling relaxations are associated with increased nebulosity and reduced incoming solar radiation). By analogy with the SO functioning and in agreement with the general understanding of baroclinic processes the intensity of the eddy cancellation mechanisms shall roughly scale with that of the Ekman flow, *i.e.*, we expect compensation (Marshall and Radko 2003) to occur whereby increasing upwelling winds steepens the isopycnals which increases the counteracting effect of eddies. In Fig. 11 the intensity of the eddy-induced circulation is expressed

as a fraction of the Ekman cell transport, for the particular wind strength that we chose. How that fraction actually varies depending on the wind conditions and wind spatial structure (Capet et al. 2004; Small et al. 2015; Bonino et al. 2019) would need to be investigated. Furthermore, the use of a pure flux vs. restoring condition for the surface buoyancy boundary condition, as well as the the timescale in the restoring case (Zhai and Munday 2014) may have an influence on the sensitivity of the residual overturning to wind stress changes (Abernathey et al. 2011). This needs to be investigated in future EBUS studies.

Finally, note that alongshore pressure gradient variability is another factor that can modulate upwelling intensity on synoptic, seasonal and longer time scales (Werner and Hickey 1983; Huyer et al. 1987; Colas et al. 2008; Marchesiello et al. 2010; McCabe et al. 2015; Jacox et al. 2018), frequently in the sense of an upwelling reduction. In the northern Benguela and southern Canary current sectors where the eddy cancellation is particularly weak this effect and its temporal variability may thus be difficult to discern. In the northern Humboldt the eddy cancellation is presumably stronger but still modest in magnitude ($\sim$ 10-20%, Fig. 11). Diagnostics of the eddy-induced circulation in realistic simulations for this upwelling sector tend to confirm our estimates. Maximum eddy-induced streamfunction values for summer reported in Colas et al. (2013) (see their Fig. 8) reach about 0.2 $m^2 s^{-1}$, *i.e.*, about 15% of the Ekman transport for that season. The CCS is the system where eddy cancellation is expected to be strongest and possibly cancel a large fraction of the Ekman circulation in some circumstances (up to 30-40%, Fig. 11). It is also the system where the manifestation of eddy fluxes has received the most observational attention (Shearman et al. 1999; Pallàs-Sanz et al. 2010b), including on biogeochemical tracer dynamics (Bograd and Mantyla 2005; Huyer et al. 2005; Pallàs-Sanz et al. 2010a). Two estimations of the eddy cancellation strength in the California current system can be drawn from Nagai et al. (2015) and Colas et al. (2013). Note that the two studies use very similar numerical configurations.

Counting streamfunction contours in Figs. 5a, b of Nagai et al. (2015) gives an annual mean eddy cancellation intensity ~ 2/8=25% of the Ekman flow at 50 m depth and 100 km from shore for central California. Slightly weaker but comparable values of 10 to 15 % are obtained in Colas et al. (2013) for summer, when upwelling winds and air-sea heat fluxes are most positive. Both estimates are within the range of values inferred from the present study.

5. Summary and conclusion

An idealized numerical model is used to study the effect of eddies on the (along-shore) mean transport of buoyancy in a coastal upwelling. The eddy contribution to buoyancy advection tends to counteract the advection by the Ekman transport, so as to limit the slope of the isopycnals. The efficiency of this eddy cancellation process varies with the strength of the air-sea buoyancy flux forcing: eddies are most effective at impeding the transport of buoyancy by Ekman currents in situations where air-sea buoyancy fluxes provide no or limited warming of upwelled surface waters drifting offshore, which allows more intense and deeper-reaching frontal conditions to be produced. Limitations imposed by our idealized framework do not allow us to work in steady state and limit the duration of our experiments to periods of tens of days. However, drifts in the thermohaline structure of our simulations remain small and our results can be interpreted using a steady-state Walin type reasoning (Marshall 1997): given the mean frontal thermohaline structure of an upwelling system vanishing (or negative) air-sea buoyancy fluxes would imply that the surface Ekman flow produces diapycnal transport of mass unless it is counteracted by eddy transport, resulting in partial or total cancellation of the mean buoyancy advection by the Ekman flow. Two limit cases and an intermediate situation are represented in Fig. 1. Our simulations fall in between the intermediate case and the total cancellation case. Concerned by the methodological limitations inherent to eddy flux estimations and descriptions we used 3 different standard methods

and found good agreement between them in our idealized setting. Identifying and quantifying eddy cancellation in realistic model simulations is far more difficult, mainly because the along-shore periodicity of our numerical configuration offers a much simpler framework for analyses. It also limits the time-averaging and/or ensemble run size requirements in a context where stochastic variability is important and can blur the role of eddies and its sensitivity to forcings. However the simplifications we take advantage of have important implications in terms of model realism. As thoroughly discussed in the previous section, the real ocean behaviour is expected to differ, with much smaller eddy effects in terms of Ekman flow cancellation than the ones we reported. Despite this important caveat, we think that the idealized posing on which the present work is based is useful to develop intuition on the role of eddies in upwelling systems. In the same spirit, a follow-up study attempting to gain insight into biogeochemical tracer dynamics is in progress. More realistic EBUS studies on eddy cancellation would be useful to further clarify the eddy role on tracer transport and distribution in EBUS, as pursued in the context of subtropical gyres by Doddridge et al. (2016) and Doddridge and Marshall (2018).

Acknowledgments. ST received funding be the European Commission (Horizon 2020, MSCA-IF-2016, WACO 749699: Fine-scale Physics, Biogeochemistry and Climate Change in the West African Coastal Ocean). ST further acknowledges support by the DFG project SFB 754 and the Excellence Cluster: Future Ocean Kiel IMAP PostDoc network respectively for two research visits at LOCEAN in Paris in 2016 and 2017. Model simulations were performed on the CINES Occigen HPC under DARI projects Dynamique et Couplage de l'Océan de surface A0050101140 and A0060101140. We thank F. Colas for providing detailed information on streamfunction estimates and fruitful discussions which helped to improve the manuscript.

Data availability statement. The overall size of the model output of all ensemble runs used for this publication is 2.7 TB. This large size makes it impossible for us to provide a constant online data access. Instead the simulations are stored safely by the first author and can be made available on request.

APPENDIX

In this appendix, we mainly repeat the derivation of Marshall and Radko (2003) in the context of an upwelling system We start with the advection-diffusion equation for the evolution of buoyancy b

$$\frac{\partial b}{\partial t} + \mathbf{u} \cdot \nabla b = D(b) \tag{A1}$$

where $\mathbf{u}$ is the 3D velocity field and D is a 3D diffusion operator

We then introduce a Reynold averaging operator (alongshore averaging) to separate rapid turbulent fluctuations from the slower part of the flow

$$X = \overline{X} + X' \tag{A2}$$

The equation of evolution for the low-passed buoyancy writes:

$$\frac{\partial \overline{b}}{\partial t} + \overline{\mathbf{u}} \cdot \nabla \overline{b} = -\boldsymbol{\nabla} \cdot \overline{\mathbf{u}' b'} + \overline{D(b)} \tag{A3}$$

Turbulence provides an additional term that we have placed in the rhs of Eq. (A3) but part of this term can actually be rewritten as advection of mean buoyancy by an eddy induced velocity field. Following Held and Schneider (1999) or Marshall and Radko (2003), and taking advantage of the alongshore periodicity of our upwelling channel (which makes the eddy flux component in that direction $\overline{u'b'}$ irrelevant), the eddy flux is decomposed into an along-isopycnal component plus a leftover as follows (see Colas et al. 2013 for an alternative decomposition with purely

along-isopycnal and diapycnal components) :

$$\left(\overline{v'b'}, \overline{w'b'}\right) = \left(\overline{w'b'}/s_{\overline{b}}, \overline{w'b'}\right) + \mathbf{F}_b \tag{A4}$$

where $s_{\overline{b}} = -\frac{\overline{b}_y}{\overline{b}_z}$ is the isopycnal slope and $\mathbf{F}_b = \left(\overline{v'b'} - \overline{w'b'}/s_{\overline{b}}, 0\right)$ is an associated diapycnal eddy flux component. (A4) can be rewritten with the help of an eddy-induced vector streamfunction

$$\mathbf{\Psi}_{Eddy}^{TEM} = \frac{\overline{w'b'}}{\overline{b}_y}\boldsymbol{i}, \tag{A5}$$

where $\boldsymbol{i}$ is the unit vector in the alongshore direction as:

$$\left(\overline{v'b'}, \overline{w'b'}\right) = \mathbf{\Psi}_{Eddy}^{TEM} \times \left(\overline{b}_y, \overline{b}_z\right) + \mathbf{F}_b\,. \tag{A6}$$

Finally, taking the divergence of (A6), (A3) can thus be rewritten:

$$\frac{\partial \overline{b}}{\partial t} + (\overline{v} + v^*)\,\overline{b}_y + (\overline{w} + w^*)\,\overline{b}_z = \overline{D(b)} - \boldsymbol{\nabla}\cdot\mathbf{F}_b \tag{A7}$$

with the so-called "bolus" velocities defined as

$$(v^*, w^*) = \boldsymbol{\nabla}\times\mathbf{\Psi}_{Eddy}^{TEM}, \tag{A8}$$

In the situation of a 2D laminar and steady-state upwelling where the Ekman circulation is the only flow component, Eq. (A7) can be written:

$$\overline{v}\overline{b}_y + \overline{w}\overline{b}_z = \overline{D(b)} \tag{A9}$$

Integrating vertically over the mixed layer in which the buoyancy gradient is supposed to be horizontal (no vertical stratification) and independent of depth, and neglecting heat, we find:

$$V_{ek}\,\left(\overline{b}_y\right)_{ml} = \overline{B_{ml}}(y) \tag{A10}$$

where $\overline{B}^{ml}$ is the net buoyancy input to the mixed layer and V_{ek} is the Ekman transport. This relationship may seem to exert a strong constraint on the mean upper ocean thermohaline structure

of upwelling systems because given the wind and buoyancy forcings $\left(\overline{b}_y\right)_{ml}$ would need to adjust so that the left- and right-hand side can match. Over relatively short study periods (40 days for the analyses we carried out) temporal tendency could contribute to the balance but we do not find this term to be important. In contrast we find that the eddies play an important role so that the neglect of the bolus velocity in (A9) is invalid (this is also the case in Southern Ocean). In real upwelling systems the eddy terms are not as strong (see Sec. 4) but the upper ocean buoyancy balance can also involve mean alongshore advection term because of lack of periodicity.

References

Abernathey, R., J. Marshall, and D. Ferreira, 2011: The dependence of southern ocean meridional overturning on wind stress. *Journal of Physical Oceanography*, **41 (12)**, 2261–2278.

Bakun, A., D. B. Field, A. REDONDO-RODRIGUEZ, and S. J. WEEKS, 2010: Greenhouse gas, upwelling-favorable winds, and the future of coastal ocean upwelling ecosystems. *Global Change Biology*, **16 (4)**, 1213–1228, doi:10.1111/j.1365-2486.2009.02094.x, URL https://onlinelibrary.wiley.com/doi/abs/10.1111/j.1365-2486.2009.02094.x, https://onlinelibrary.wiley.com/doi/pdf/10.1111/j.1365-2486.2009.02094.x.

Barnier, B., L. Siefridt, and P. Marchesiello, 1995: Thermal forcing for a global ocean circulation model using a three-year climatology of ecmwf analyses. *Journal of Marine Systems*, **6 (4)**, 363 – 380, doi:https://doi.org/10.1016/0924-7963(94)00034-9, URL http://www.sciencedirect.com/science/article/pii/0924796394000349.

Beardsley, R. C., E. P. Dever, S. J. Lentz, and J. P. Dean, 1998: Surface heat flux variability over the northern california shelf. *J. Geophys. Res.*, **103**, 21 553–21 586.

590 Bograd, S. J., and A. W. Mantyla, 2005: On the subduction of upwelled waters in the california
591 current. *Journal of Marine Research*, **63 (5)**, 863–885, doi:doi:10.1357/002224005774464229,
592 URL https://www.ingentaconnect.com/content/jmr/jmr/2005/00000063/00000005/art00001.

593 Bonino, G., E. Di Lorenzo, S. Masina, and I. D., 2019: Interannual to decadal variability within
594 and across the major eastern boundary upwelling systems. *Sci Rep*, **9 (19949)**, doi:https://doi.
595 org/10.1038/s41598-019-56514-8.

596 Capet, X., F. Colas, P. Penven, P. Marchesiello, and J. C. McWilliams, 2008: Eddies in eastern-
597 boundary subtropical upwelling systems. *Ocean Modeling in an Eddying Regime*, **1567**, 131–
598 147.

599 Capet, X., G. Roullet, P. Klein, and G. Maze, 2016: Intensification of upper-ocean submesoscale
600 turbulence through charney baroclinic instability. *Journal of Physical Oceanography*, **46 (11)**,
601 3365–3384, doi:10.1175/JPO-D-16-0050.1, URL https://doi.org/10.1175/JPO-D-16-0050.1,
602 https://doi.org/10.1175/JPO-D-16-0050.1.

603 Capet, X. J., P. Marchesiello, and J. C. McWilliams, 2004: Upwelling response to coastal wind
604 profiles. *Geophysical Research Letters*, **31 (13)**, doi:10.1029/2004GL020123.

605 Carton, X., 2010: *Oceanic Vortices*, 61–108. Springer Berlin Heidelberg, Berlin, Heidelberg,
606 doi:10.1007/978-3-642-11587-5_3, URL https://doi.org/10.1007/978-3-642-11587-5_3.

607 Centurioni, L. R., J. C. Ohlmann, and P. P. Niiler, 2008: Permanent meanders in the california cur-
608 rent system. *Journal of Physical Oceanography*, **38 (8)**, 1690–1710, doi:10.1175/2008JPO3746.
609 1, URL https://doi.org/10.1175/2008JPO3746.1, https://doi.org/10.1175/2008JPO3746.1.

610 Chelton, D. B., P. Gaube, M. G. Schlax, J. J. Early, and R. M. Samelson, 2011: The influence
611 of nonlinear mesoscale eddies on near-surface oceanic chlorophyll. *Science*, **334 (6054)**, 328–

332, doi:10.1126/science.1208897, URL https://science.sciencemag.org/content/334/6054/328, https://science.sciencemag.org/content/334/6054/328.full.pdf.

Colas, F., X. Capet, J. McWilliams, and A. Shchepetkin, 2008: 1997–1998 el niño off peru: A numerical study. *Progress in Oceanography*, **79 (2)**, 138 – 155, doi:https://doi.org/10.1016/j.pocean.2008.10.015, URL http://www.sciencedirect.com/science/article/pii/S0079661108001687, the Northern Humboldt Current System: Ocean Dynamics, Ecosystem Processes, and Fisheries.

Colas, F., X. Capet, J. C. McWilliams, and Z. Li, 2013: Mesoscale eddy buoyancy flux and eddy-induced circulation in eastern boundary currents. *Journal of Physical Oceanography*, **43 (6)**, 1073–1095, doi:10.1175/JPO-D-11-0241.1, URL https://doi.org/10.1175/JPO-D-11-0241.1, https://doi.org/10.1175/JPO-D-11-0241.1.

Colas, F., J. C. McWilliams, X. Capet, and J. Kurian, 2012: Heat balance and eddies in the Peru-Chile current system. *Climate Dynamics*, **39 (1-2)**, 509–529, doi:10.1007/s00382-011-1170-6.

Condie, S., and J. R. Dunn, 2006: Seasonal characteristics of the surface mixed layer in the australasian region: Implications for primary production regimes and biogeography. *Marine and Freshwater Research - MAR FRESHWATER RES*, **57**, 569–590.

Doddridge, E. W., and D. P. Marshall, 2018: Implications of eddy cancellation for nutrient distribution within subtropical gyres. *Journal of Geophysical Research: Oceans*, **123 (9)**, 6720–6735, doi:https://doi.org/10.1029/2018JC013842, URL https://agupubs.onlinelibrary.wiley.com/doi/abs/10.1029/2018JC013842, https://agupubs.onlinelibrary.wiley.com/doi/pdf/10.1029/2018JC013842.

633 Doddridge, E. W., D. P. Marshall, and A. M. Hogg, 2016: Eddy cancellation of the ekman
634 cell in subtropical gyres. *Journal of Physical Oceanography*, **46 (10)**, 2995–3010, doi:https:
635 //doi.org/10.1175/JPO-D-16-0097.1.

636 Döös, K., and D. J. Webb, 1994: The deacon cell and the other meridional cells of the southern
637 ocean. *J. Phys. Oceanogr.*, **24**, 429–442.

638 Flynn, K. R., M. R. Fewings, C. Gotschalk, and K. Lombardo, 2017: Large-scale anomalies in
639 sea-surface temperature and air-sea fluxes during wind relaxation events off the united states
640 west coast in summer. *J. Geophys. Res.*, **122**, 2574–2594.

641 Fox-Kemper, B., R. Ferrari, and R. Hallberg, 2008: Parameterization of mixed layer ed-
642 dies. part i: Theory and diagnosis. *Journal of Physical Oceanography*, **38 (6)**, 1145–1165,
643 doi:10.1175/2007JPO3792.1, URL https://doi.org/10.1175/2007JPO3792.1, https://doi.org/10.
644 1175/2007JPO3792.1.

645 Garabato, A. C. N., D. P. Stevens, A. J. Watson, and W. Roether, 2007: Short-circuiting of the
646 overturning circulation in the antarctic circumpolar current. *Nature*, **447**, 194.

647 Gent, P. R., 2016: Effects of southern hemisphere wind changes on the merid-
648 ional overturning circulation in ocean models. *Annual Review of Marine Sci-*
649 *ence*, **8 (1)**, 79–94, doi:10.1146/annurev-marine-122414-033929, URL https://doi.
650 org/10.1146/annurev-marine-122414-033929, pMID: 26163010, https://doi.org/10.1146/
651 annurev-marine-122414-033929.

652 Gruber, N., Z. Lachkar, H. Frenzel, P. Marchesiello, M. Münnich, J. C. McWilliams, T. Nagai,
653 and G.-K. Plattner, 2011: Eddy-induced reduction of biological production in eastern boundary

upwelling systems. *Nature Geoscience*, **4 (11)**, 787–792, doi:10.1038/ngeo1273, URL http://dx.doi.org/10.1038/ngeo1273.

Hallberg, R., and A. Gnanadesikan, 2006: The role of eddies in determining the structure and response of the wind-driven southern hemisphere overturning: Results from the modeling eddies in the southern ocean (meso) project. *Journal of Physical Oceanography*, **36 (12)**, 2232–2252, doi:10.1175/JPO2980.1, URL https://doi.org/10.1175/JPO2980.1, https://doi.org/10.1175/JPO2980.1.

Haney, R. L., R. A. Hale, and D. E. Dietrich, 2001: Offshore propagation of eddy kinetic energy in the california current. *Journal of Geophysical Research: Oceans*, **106 (C6)**, 11 709–11 717, doi:10.1029/2000JC000433, URL https://agupubs.onlinelibrary.wiley.com/doi/abs/10.1029/2000JC000433, https://agupubs.onlinelibrary.wiley.com/doi/pdf/10.1029/2000JC000433.

Held, I. M., and T. Schneider, 1999: The surface branch of the zonally averaged mass transport circulation in the troposphere. *Journal of the Atmospheric Sciences*, **56 (11)**, 1688–1697, doi:10.1175/1520-0469(1999)056<1688:TSBOTZ>2.0.CO;2, URL https://doi.org/10.1175/1520-0469(1999)056<1688:TSBOTZ>2.0.CO;2, https://doi.org/10.1175/1520-0469(1999)056<1688:TSBOTZ>2.0.CO;2.

Huyer, A., J. H. Fleischbein, J. Keister, P. M. Kosro, N. Perlin, R. L. Smith, and P. A. Wheeler, 2005: Two coastal upwelling domains in the northern california current system. *J. Mar. Res.*, **63**, 901–929.

Huyer, A., R. L. Smith, and T. Paluszkiewicz, 1987: Coastal upwelling off peru during normal and el nino times, 1981–1984. *J. Geophys. Res.*, **92**, 14 297–14 307.

Jacox, M. G., C. A. Edwards, E. L. Hazen, and S. J. Bograd, 2018: Coastal upwelling revisited: Ekman, bakun, and improved upwelling indices for the u.s. west coast. *Journal of Geophysical Research: Oceans*, **123 (10)**, 7332–7350, doi:10.1029/2018JC014187, URL https://agupubs.onlinelibrary.wiley.com/doi/abs/10.1029/2018JC014187, https://agupubs.onlinelibrary.wiley.com/doi/pdf/10.1029/2018JC014187.

Johnston, T. S., and D. L. Rudnick, 2009: Observations of the transition layer. *J. Phys. Oceanogr.*, **39**, 780–797.

Karsten, R. H., and J. Marshall, 2002: Constructing the residual circulation of the acc from observations. *Journal of Physical Oceanography*, **32 (12)**, 3315–3327, doi:10.1175/1520-0485(2002)032<3315:CTRCOT>2.0.CO;2, URL https://doi.org/10.1175/1520-0485(2002)032<3315:CTRCOT>2.0.CO;2, https://doi.org/10.1175/1520-0485(2002)032<3315:CTRCOT>2.0.CO;2.

Large, W. G., J. C. McWilliams, and S. C. Doney, 1994: Oceanic vertical mixing: A review and a model with a nonlocal boundary layer parameterization. *Reviews of Geophysics*, **32 (4)**, 363–403, doi:10.1029/94RG01872, URL https://agupubs.onlinelibrary.wiley.com/doi/abs/10.1029/94RG01872, https://agupubs.onlinelibrary.wiley.com/doi/pdf/10.1029/94RG01872.

Lathuilière, C., V. Echevin, M. Lévy, and G. Madec, 2010: On the role of the mesoscale circulation on an idealized coastal upwelling ecosystem. *Journal of Geophysical Research: Oceans*, **115 (9)**, 1–14, doi:10.1029/2009JC005827.

Lee, M.-M., and A. J. G. Nurser, 2012: Eddy subduction and the vertical transport streamfunction. *Journal of Physical Oceanography*, **42 (11)**, 1762–1780, doi:10.1175/JPO-D-11-0219.1, URL https://doi.org/10.1175/JPO-D-11-0219.1, https://doi.org/10.1175/JPO-D-11-0219.1.

Lemarié, F., J. Kurian, A. F. Shchepetkin, M. Jeroen Molemaker, F. Colas, and J. C. McWilliams, 2012: Are there inescapable issues prohibiting the use of terrain-following coordinates in climate models? *Ocean Modelling*, **42**, 57–79, doi:https://doi.org/10.1016/j.ocemod.2011.11.007, URL https://www.sciencedirect.com/science/article/pii/S1463500311001831.

Lentz, S. J., and D. C. Chapman, 2004: The importance of nonlinear cross-shelf momentum flux during wind-driven coastal upwelling. *Journal of Physical Oceanography*, **34 (11)**, 2444–2457, doi:10.1175/JPO2644.1, URL https://doi.org/10.1175/JPO2644.1, https://doi.org/10.1175/JPO2644.1.

Lübbecke, J. F., P. Brandt, M. Dengler, R. Kopte, J. Lüdke, I. Richter, M. S. Martins, and P. C. Tchipalanga, 2019: Causes and evolution of the southeastern tropical atlantic warm event in early 2016. *Climate Dynamics*, **53**, 261–274.

Mak, J., D. P. Marshall, J. R. Maddison, and S. D. Bachman, 2017: Emergent eddy saturation from an energy constrained eddy parameterisation. *Ocean Modelling*, **112**, 125–138.

Marchesiello, P., L. Debreu, and X. Couvelard, 2009: Spurious diapycnal mixing in terrain-following coordinate models: The problem and a solution. *Ocean Modelling*, **26 (3)**, 156–169, doi:https://doi.org/10.1016/j.ocemod.2008.09.004, URL https://www.sciencedirect.com/science/article/pii/S1463500308001510.

Marchesiello, P., J. Lefèvre, A. Vega, X. Couvelard, and C. Menkes, 2010: Coastal upwelling, circulation and heat balance around new caledonia's barrier reef. *Marine Pollution Bulletin*, **61 (7)**, 432 – 448, doi:https://doi.org/10.1016/j.marpolbul.2010.06.043, URL http://www.sciencedirect.com/science/article/pii/S0025326X10002869, new Caledonia tropical lagoons: an overview of multidisciplinary investigations.

718 Marchesiello, P., J. C. McWilliams, and A. Shchepetkin, 2003: Equilibrium structure and
719 dynamics of the california current system. *Journal of Physical Oceanography*, **33 (4)**,
720 753–783, doi:10.1175/1520-0485(2003)33<753:ESADOT>2.0.CO;2, URL https://doi.org/10.
721 1175/1520-0485(2003)33<753:ESADOT>2.0.CO;2, https://doi.org/10.1175/1520-0485(2003)
722 33<753:ESADOT>2.0.CO;2.

723 Marshall, D., 1997: Subduction of water masses in an eddying ocean. *Journal of Marine Research*,
724 **55 (2)**, 201–222, doi:doi:10.1357/0022240973224373, URL https://www.ingentaconnect.com/
725 content/jmr/jmr/1997/00000055/00000002/art00002.

726 Marshall, D. P., J. R. Maddison, and P. S. Berloff, 2012: A framework for parameterizing eddy
727 potential vorticity fluxes. *J. Phys. Oceanogr.*, **42**, 539–557.

728 Marshall, J., and T. Radko, 2003: Residual-mean solutions for the antarctic circumpolar current
729 and its associated overturning circulation. *J. Phys. Oceanogr.*, **33**, 2341–2354.

730 Marshall, J., and T. Radko, 2006: A model of the upper branch of the meridional over-
731 turning of the southern ocean. *Progress in Oceanography*, **70 (2)**, 331 – 345, doi:https://
732 doi.org/10.1016/j.pocean.2006.07.004, URL http://www.sciencedirect.com/science/article/pii/
733 S007966110600084X, gabriel T. Csanady: Understanding the Physics of the Ocean.

734 Marshall, J., and K. Speer, 2012: Closure of the meridional overturning circulation through
735 southern ocean upwelling. *Nature Geoscience*, **5 (5)**, 171–180, doi:10.1038/ngeo1391, URL
736 doi:10.1038/ngeo1391.

737 McCabe, R. M., B. M. Hickey, E. P. Dever, and P. MacCready, 2015: Seasonal cross-
738 shelf flow structure, upwelling relaxation, and the alongshelf pressure gradient in the north-

ern california current system. *Journal of Physical Oceanography*, **45 (1)**, 209–227, doi: 10.1175/JPO-D-14-0025.1, URL https://doi.org/10.1175/JPO-D-14-0025.1.

Morrison, A. K., A. M. Hogg, and M. L. Ward, 2011: Sensitivity of the southern ocean overturning circulation to surface buoyancy forcing. *Geophysical Research Letters*, **38 (14)**, doi:10.1029/2011GL048031, URL https://agupubs.onlinelibrary.wiley.com/doi/abs/10.1029/2011GL048031, https://agupubs.onlinelibrary.wiley.com/doi/pdf/10.1029/2011GL048031.

Nagai, T., N. Gruber, H. Frenzel, Z. Lachkar, J. C. McWilliams, and G.-K. Plattner, 2015: Dominant role of eddies and filaments in the offshore transport of carbon and nutrients in the california current system. *Journal of Geophysical Research: Oceans*, **120 (8)**, 5318–5341.

Ndoye, S., X. Capet, P. Estrade, B. Sow, E. Machu, T. Brochier, J. Döring, and P. Brehmer, 2017: Dynamics of a "low-enrichment high-retention" upwelling center over the southern senegal shelf. *Geophysical Research Letters*, **44 (10)**, 5034–5043, doi:https://doi.org/10.1002/2017GL072789, URL https://agupubs.onlinelibrary.wiley.com/doi/abs/10.1002/2017GL072789, https://agupubs.onlinelibrary.wiley.com/doi/pdf/10.1002/2017GL072789.

Nurser, A. J. G., and M.-M. Lee, 2004a: Isopycnal averaging at constant height. part i: The formulation and a case study. *Journal of Physical Oceanography*, **34 (12)**, 2721–2739, doi:10.1175/JPO2649.1, URL https://doi.org/10.1175/JPO2649.1, https://doi.org/10.1175/JPO2649.1.

Nurser, A. J. G., and M.-M. Lee, 2004b: Isopycnal averaging at constant height. part ii: Relating to the residual streamfunction in eulerian space. *Journal of Physical Oceanography*, **34 (12)**, 2740–2755, doi:10.1175/JPO2650.1, URL https://doi.org/10.1175/JPO2650.1, https://doi.org/10.1175/JPO2650.1.

Pallàs-Sanz, E., T. Johnston, and D. Rudnick, 2010a: Frontal dynamics in a california current system shallow front: 1. frontal processes and tracer structure. *J. Geophys. Res.*, **115**.

Pallàs-Sanz, E., T. Johnston, and D. Rudnick, 2010b: Frontal dynamics in a california current system shallow front: 2. mesoscale vertical velocity. *Journal of Geophysical Research: Oceans*, **115 (C12)**.

Praveen Kumar, B., J. Vialard, M. Lengaigne, V. S. N. Murty, and M. J. McPhaden, 2012: Tropflux: air-sea fluxes for the global tropical oceans description and evaluation. *Climate Dynamics*, **38 (7)**, 1521–1543, doi:10.1007/s00382-011-1115-0, URL https://doi.org/10.1007/s00382-011-1115-0.

Ridgway, K., J. R. Dunn, and J. Wilkin, 2002: Ocean interpolation by four-dimensional weighted least squares—application to the waters around australasia. *Journal of Atmospheric and Oceanic Technology*, **19**, 1357–1375.

Send, U., R. C. Beardsley, and C. D. Winant, 1987: Relaxation from upwelling in the coastal ocean dynamics experiment. *J. Geophys. Res.*, **92**, 1683–1698.

Shchepetkin, A. F., and J. C. McWilliams, 2009: Correction and commentary for "ocean forecasting in terrain-following coordinates: Formulation and skill assessment of the regional ocean modeling system" by haidvogel et al., j. comp. phys. 227, pp. 3595–3624. *Journal of Computational Physics*, **228 (24)**, 8985–9000, doi:https://doi.org/10.1016/j.jcp.2009.09.002, URL https://www.sciencedirect.com/science/article/pii/S0021999109004872.

Shearman, R. K., J. A. Barth, and P. M. Kosro, 1999: Diagnosis of the three-dimensional circulation associated with mesoscale motion in the california current. *J. Phys. Oceanogr.*, **29**, 651–670.

781 Silvester, J. M., Y.-D. Lenn, J. A. Polton, T. P. Rippeth, and M. M. Maqueda, 2014: Observations
782 of a diapycnal shortcut to adiabatic upwelling of antarctic circumpolar deep water. *Geophys.*
783 *Res. Lett.*, **41**, 7950–7956.

784 Small, R. J., E. Curchitser, K. Hedstrom, B. Kauffman, and W. G. Large, 2015: The benguela
785 upwelling system: Quantifying the sensitivity to resolution and coastal wind representation in
786 a global climate model. *Journal of Climate*, **28 (23)**, 9409–9432, doi:https://doi.org/10.1038/
787 s41598-019-56514-8.

788 Walin, G., 1982: On the relation between sea-surface heat flow and thermal circu-
789 lation in the ocean. *Tellus*, **34 (2)**, 187–195, doi:10.1111/j.2153-3490.1982.tb01806.
790 x, URL https://onlinelibrary.wiley.com/doi/abs/10.1111/j.2153-3490.1982.tb01806.x, https://
791 onlinelibrary.wiley.com/doi/pdf/10.1111/j.2153-3490.1982.tb01806.x.

792 Werner, F. E., and B. M. Hickey, 1983: The role of a longshore pressure gradient in pacific
793 northwest coastal dynamics. *JPO*, **13**, 395–410.

794 Zhai, X., and D. R. Munday, 2014: Sensitivity of southern ocean overturning to wind stress
795 changes: Role of surface restoring time scales. *Ocean Modelling*, **84**, 12–25, doi:https:
796 //doi.org/10.1016/j.ocemod.2014.09.004, URL https://www.sciencedirect.com/science/article/
797 pii/S1463500314001358.

LIST OF TABLES

801 TABLE 1. Model run acronyms, horizontal resolution, number of grid cells, time steps, duration, ensemble
802 number, heat flux parameter dQ/dt and wind stress.

Acronym	Δx, m	grid cells (x, y, z)	time step, s	duration, days	ensembles	dQ/dT, $W m^{-2} K^{-1}$	wind stress, $N m^{-2}$
Submesoscale No Flux, NF	794	504, 756, 100	80	80	12	0	0.075
Submesoscale Medium Flux, MF	794	504, 756, 100	80	80	12	- 25	0.075
Submesoscale High Flux, HF	794	504, 756, 100	80	80	12	- 50	0.075
Mesoscale No Flux, NF	8000	50, 75, 100	540	80	12	0	0.075
Mesoscale Medium Flux, MF	8000	50, 75, 100	540	80	12	- 25	0.075
Mesoscale High Flux, HF	8000	50, 75, 100	540	80	12	- 50	0.075

LIST OF FIGURES

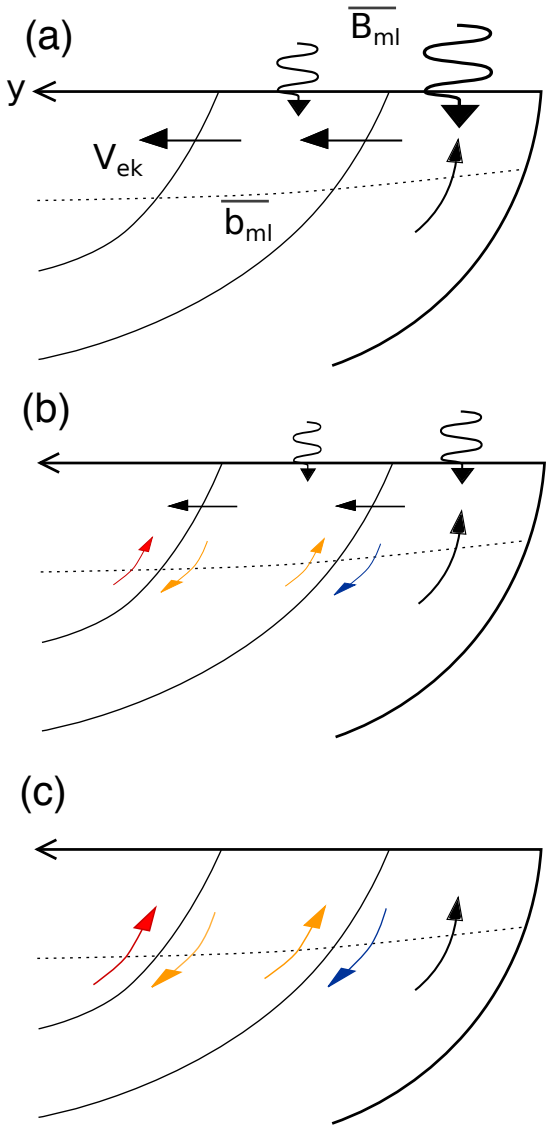

FIG. 1. Schematic showing the effect of atmospheric buoyancy forcing ($\overline{B_{ml}}$) on the cross-shore circulation in upwelling regimes. The offshore Ekman transport (v_{ek}) is shown in black arrows. The strength of eddy cancellation is sketched with colored arrows with blue representing colder upwelled water and red warmer offshore waters. Case (a) represents the traditional view of upwelling systems, (b) is consistent with the typical Southern Ocean conception including eddy cancellation and (c) represents an extreme situation where vanishing buoyancy flux and intense eddy activity lead to full cancellation. Note that the 3 idealized cases of this study fall in between b and c. The coast is located in $y = 0$.

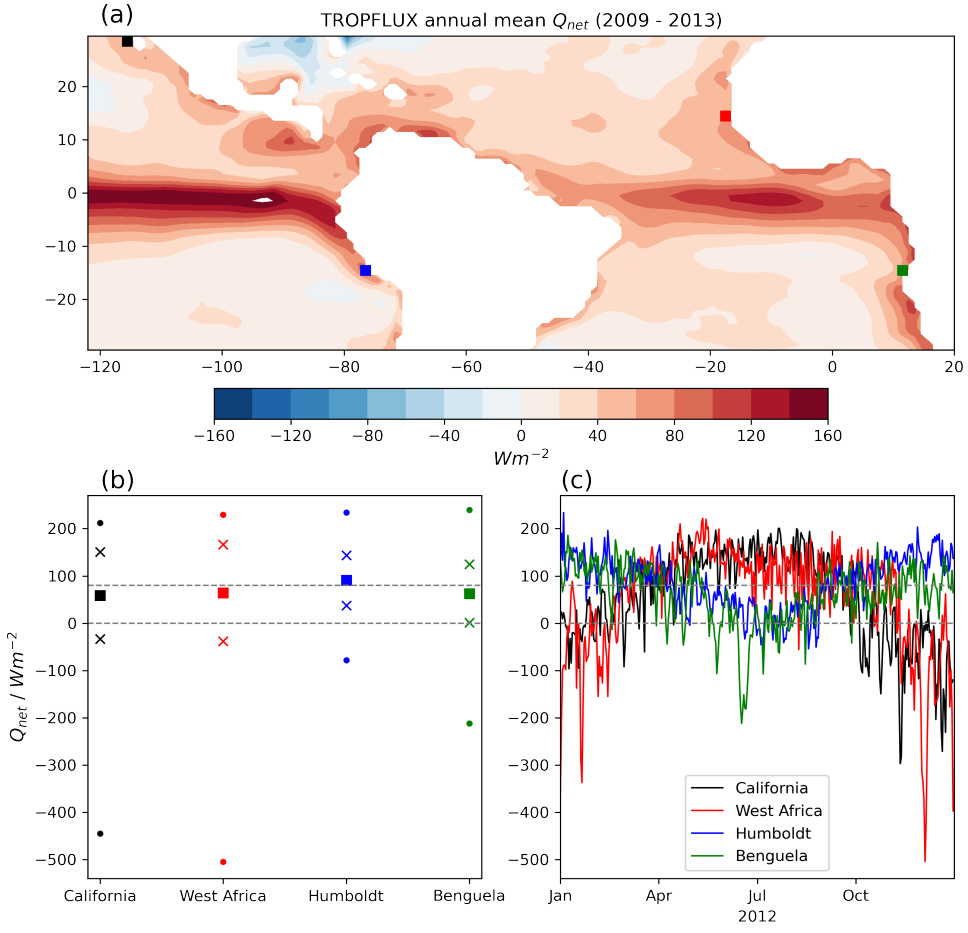

FIG. 2. Annual mean net buoyancy flux for 2009 to 2013 period from TropFlux (Praveen Kumar et al. 2012) (a). The four eastern boundary upwelling systems (EBUS): California, West Africa, Humboldt and Benguela are marked with black, red, blue and green squares (a). Annual mean (squares) heat fluxes, standard deviation (crosses) and maximum and minimum (dots) for the four EBUS Systems for the 2009 to 2013 period (b). Daily net buoyancy fluxes for each EBUS system for 2012 (c). The TropFlux data is produced under a collaboration between Laboratoire d'Océanographie: Expérimentation et Approches Numériques (LOCEAN) from Institut Pierre Simon Laplace (IPSL, Paris, France) and National Institute of Oceanography/CSIR (NIO, Goa, India), and supported by Institut de Recherche pour le Développement (IRD, France). TropFlux relies on data provided by the ECMWF Re-Analysis interim (ERA-I) and ISCCP projects. The vertical dashed black lines in b and c indicate the parameter space (0 - 80 W/m^{-2}) explored in this idealized study.

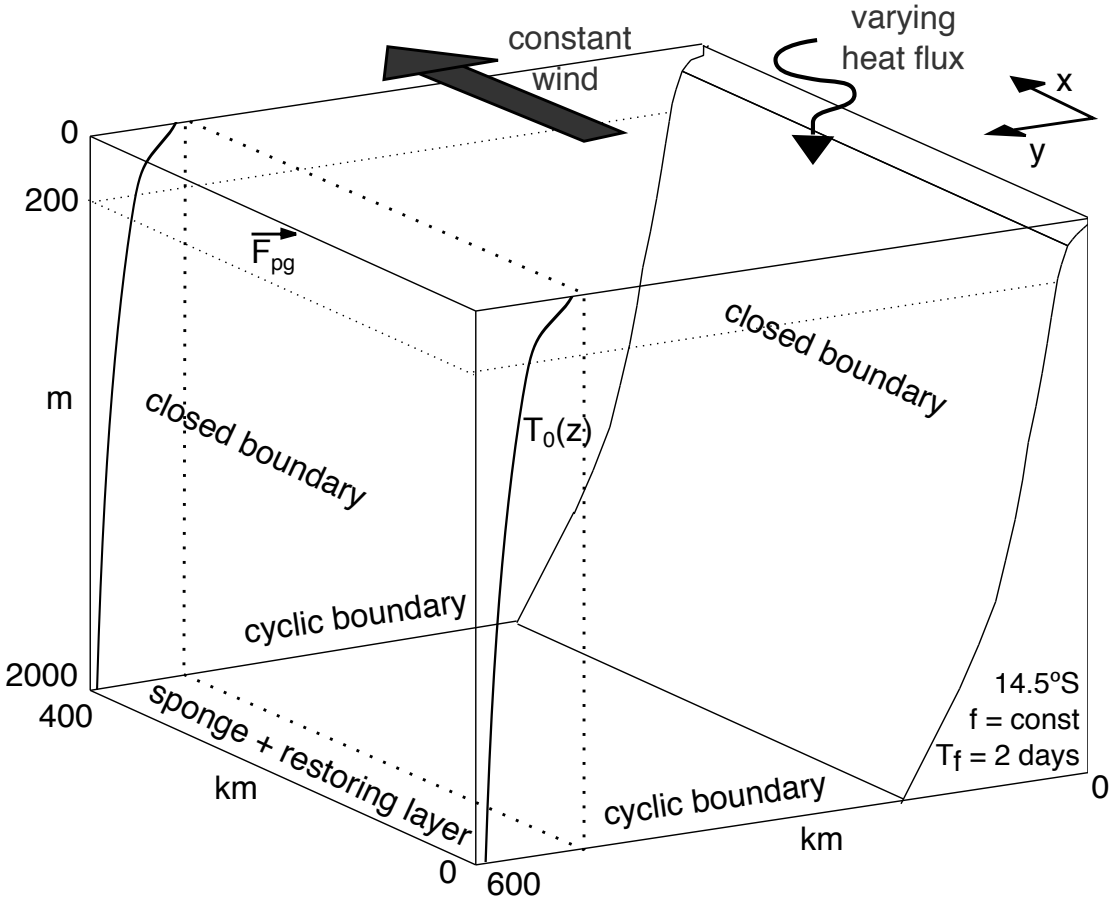

FIG. 3. Schematic of idealized eastern boundary upwelling model configuration. Model setup and schematic were inspired by Lathuilière et al. (2010). The model grid consists of a shallow shelf, a continental slope and a flat bottom. The Coriolis parameter (f) is constant and corresponds to a latitude of 14.5°S. The surface ocean is forced with a constant wind stress of 0.075 Nm^{-2} and varying heat fluxes (details in section 2 b). A sponge layer exists offshore with enhanced diffusivity and viscosity coefficients. There full depth temperatures are restored to the initial temperature profile $T_o(z)$ (see Eq. (3)). An alongshore pressure gradient is prescribed in the upper 200 m which drives an onshore flow balancing the offshore Ekman transport.

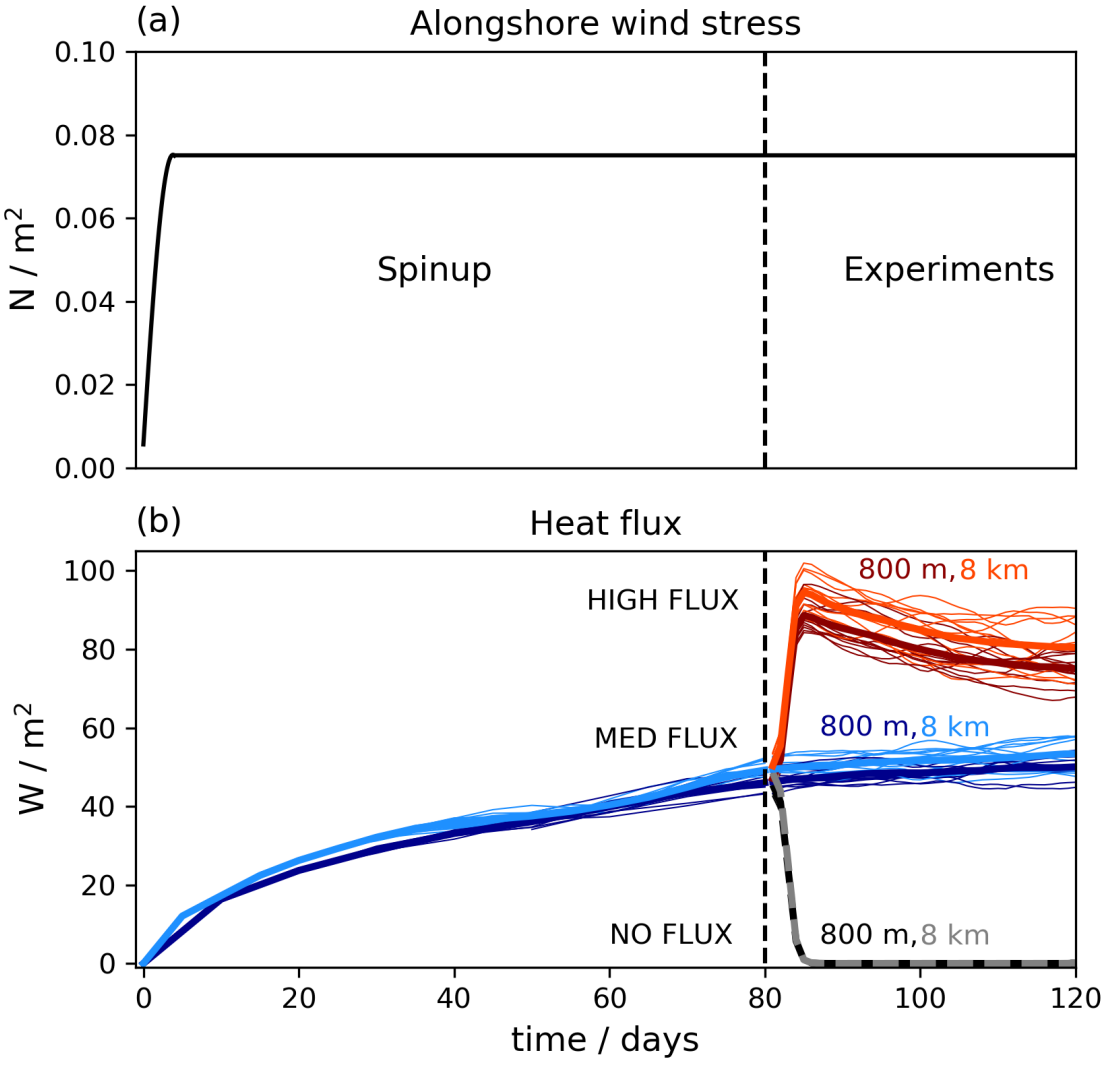

907 FIG. 4. Domain averaged wind stress (a) and heat flux (b) forcing during the model spin-up (day 0 to 80) and
908 the three different heat flux experiments (day 80 to 120). The NF, MF and HF experiments are shown in black
909 / gray, dark / light blue and dark / light red for the submesoscale (Δx = 800m) and mesoscale (Δx = 8 km) runs
910 respectively. Single runs and ensemble mean are shown in thin and thick lines respectively.

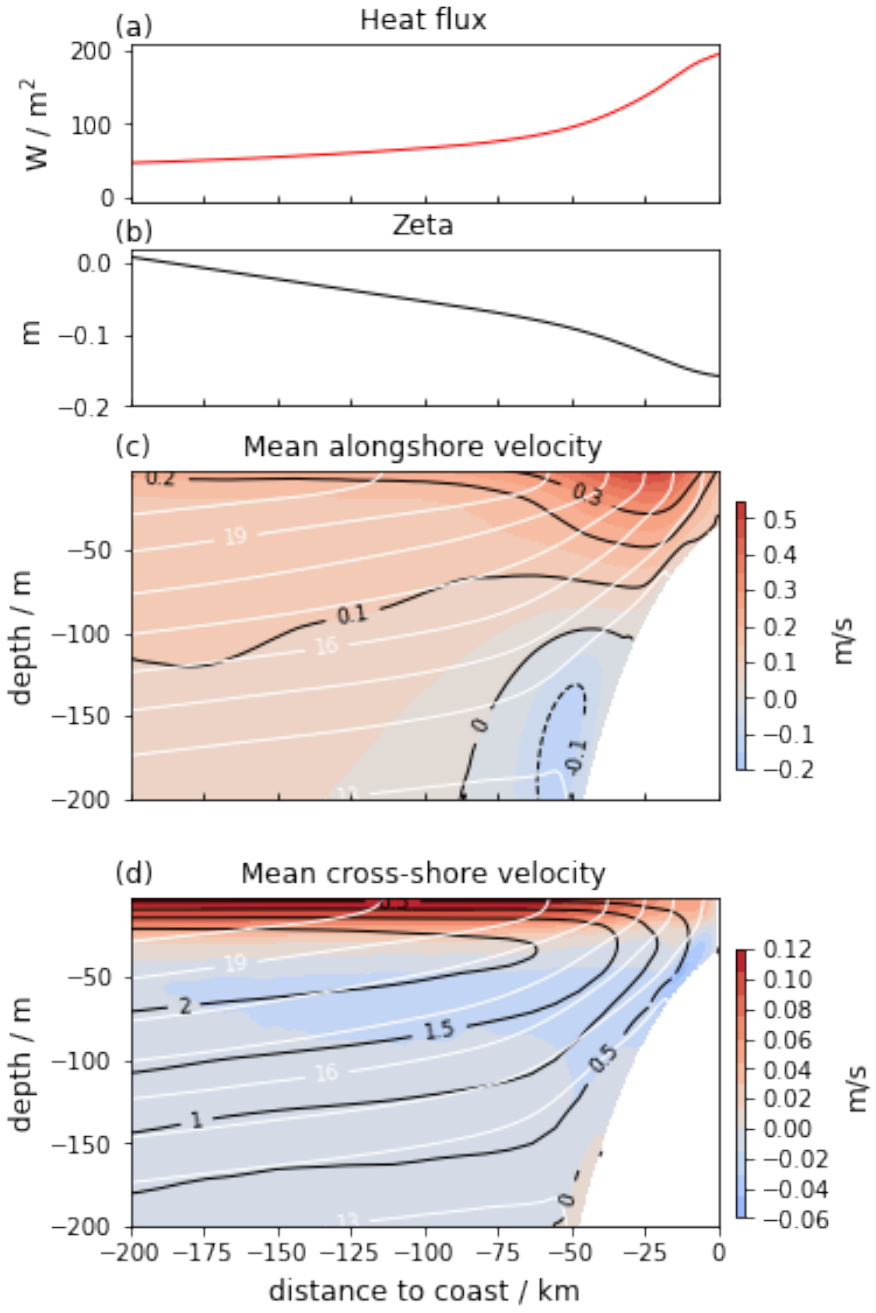

911 FIG. 5. Temporal-mean alongshore-averaged heat flux (a), zeta (b), alongshore (c) and crosshore circulation
912 (d) in reference simulation (MF) averaged over the time of the experiments (day 81 to day 120). Isothermes are
913 contoured in white (c, d). Eulerian mean streamfunction is shown in black contours (d).

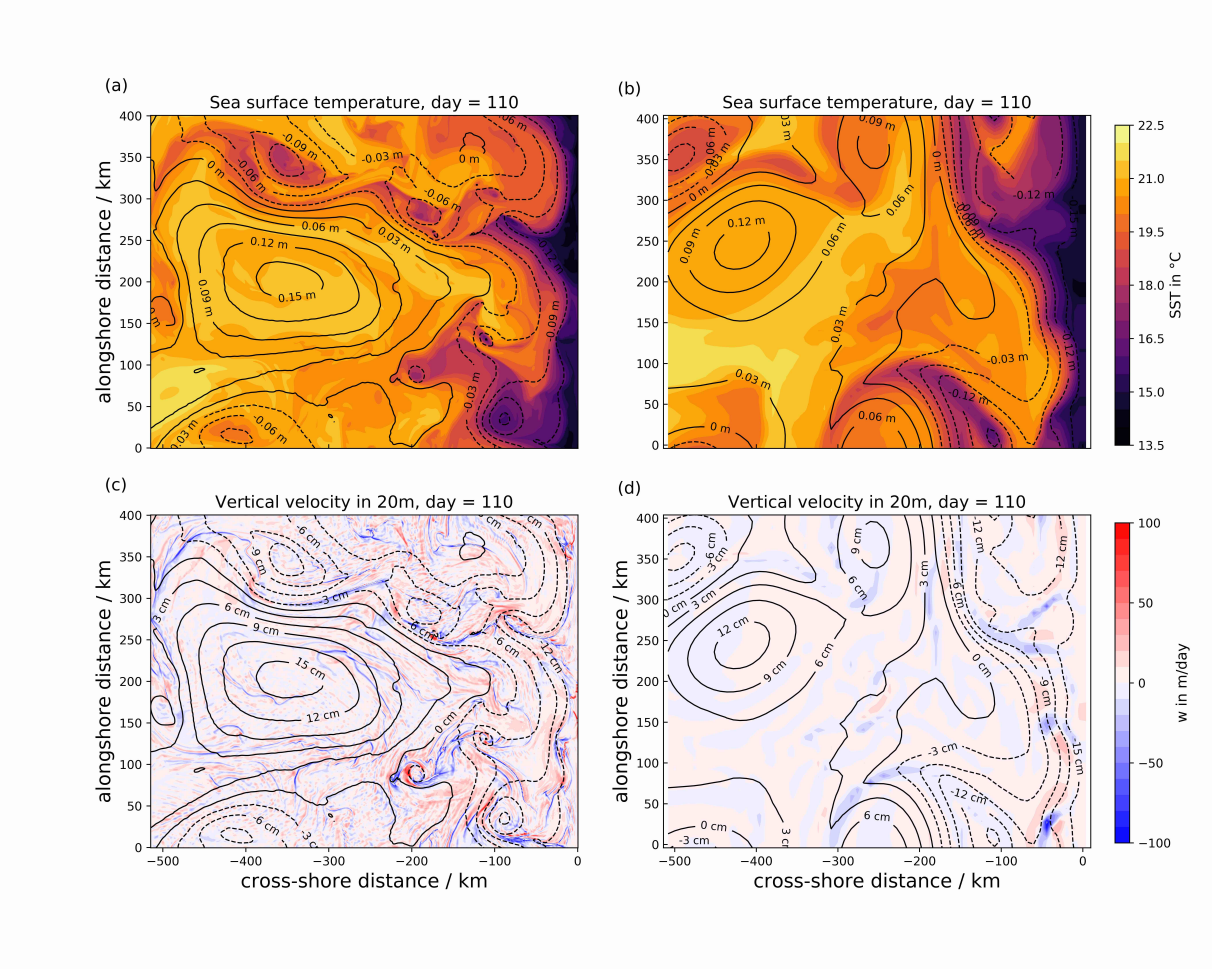

914 FIG. 6. Sea surface temperature (SST, in $°C$) (a, b) and vertical velocities in m/day (c, d) in 20 m depth at day
915 110 for medium heat flux forcing for submesoscale (Δx = 800 m, a, c) and mesoscale (Δx = 8 km, b, d) horizontal
916 resolution respectively. Sea level anomaly (zeta) in cm is shown in black contours.

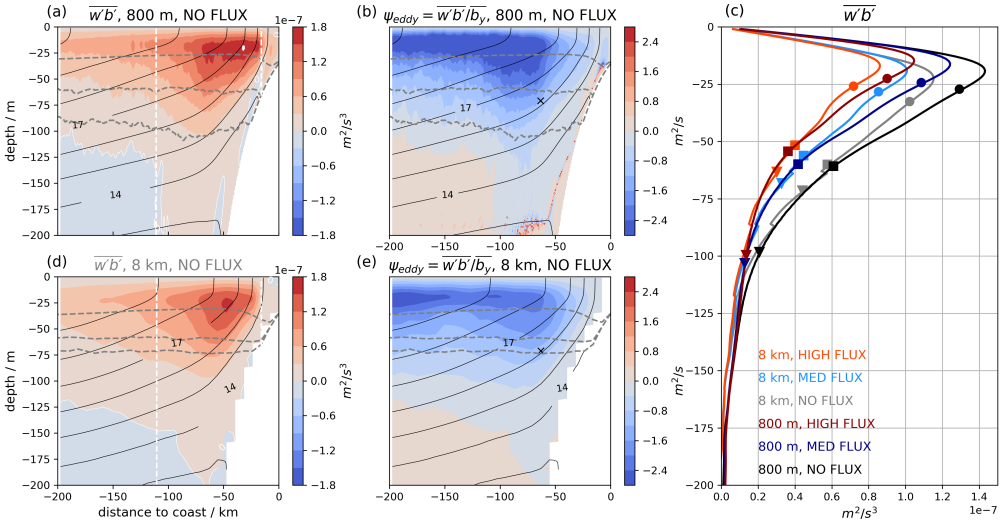

FIG. 7. Ensemble mean vertical eddy buoyancy fluxes (a, d) and eddy streamfunctions based on transformed Eulerian mean theory (Ψ^{TEM}_{eddy}) (b,d) for NF experiments (day = 81 to 120) at submesoscale (Δx = 800 m) and mesoscale (Δx = 8 km) horizontal resolution respectively. Ensemble mean vertical eddy buoyancy fluxes averaged between 16 to 112 km (white dashed lines in a and d) from the coast (c). The mean, 95 percentile and maximum mixed layer depth of all 12 ensembles averages are shown in gray dashed lines (a, b, d, e) and as averages between 16 to 112 km with filled circles, squares and triangles in c respectively.

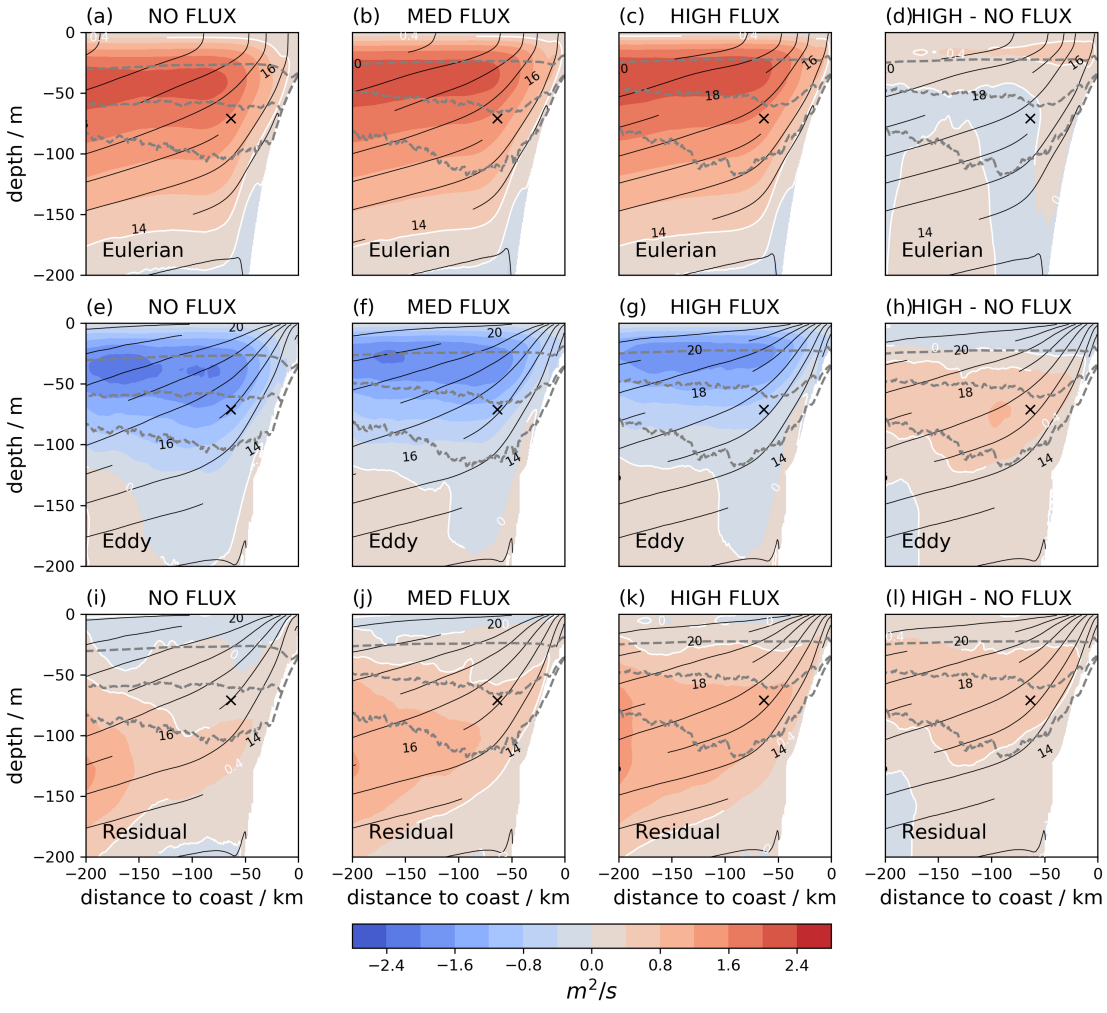

FIG. 8. Eulerian Ψ^{iso-h}_{Mean} (a, b, c, d), eddy Ψ^{iso-h}_{Eddy} (e, f, g, h) and residual Ψ^{iso-h}_{Res} (i, j, k, l) streamfunctions in m^2/s during NF (a, e, i), MF (b, f, j) and HF (c, g, k) air-sea buoyancy forcing. The last column shows the difference between HF and NF forcing experiments. Isotherms are contoured every 1°C in black. The mean, 95 percentile and maximum mixed layer depth are shown in gray dashed lines. The black cross marks the position of the streamfunction strengths shown in Figure 10.

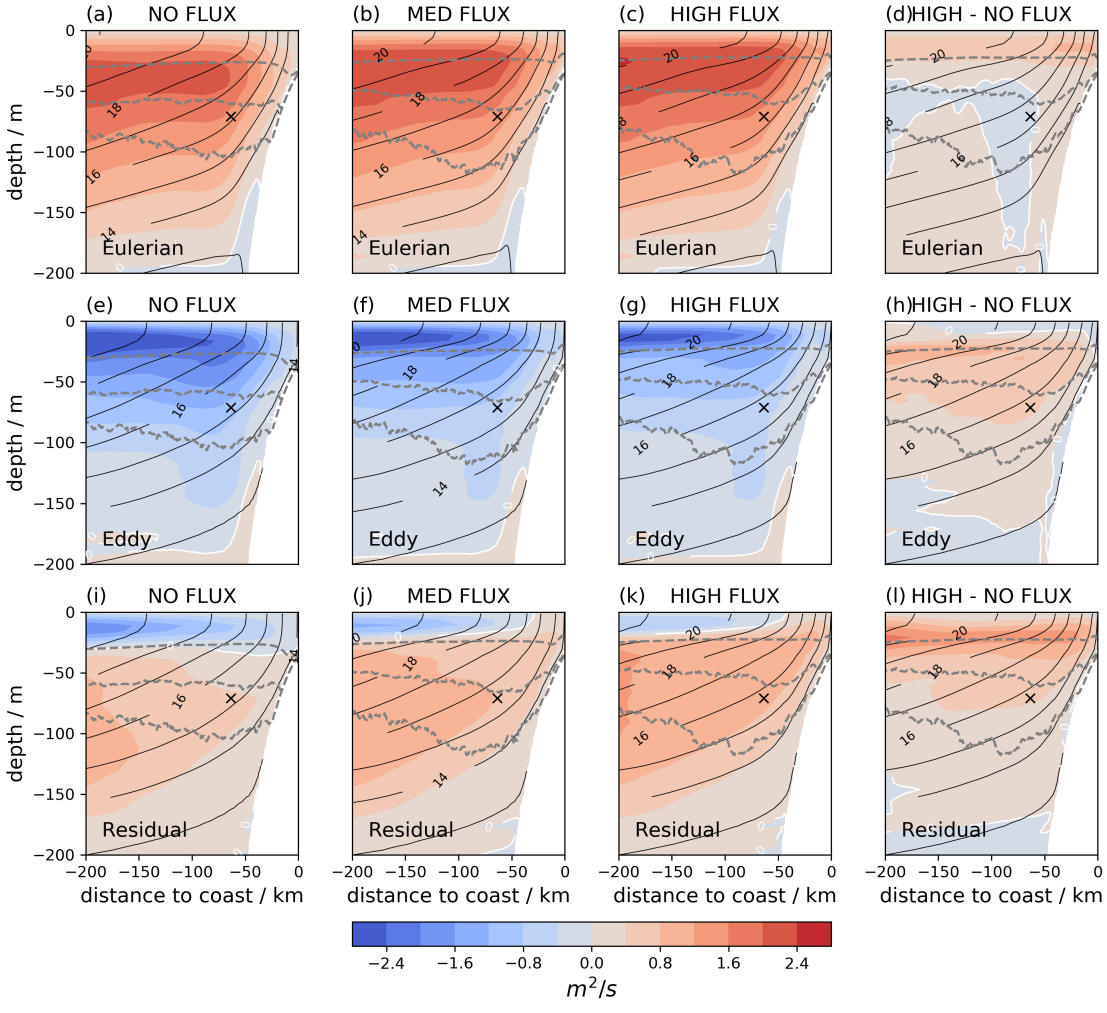

FIG. 9. Same as Fig. 8 but for Ψ^{iso-v}_{Mean}, Ψ^{iso-v}_{Eddy} and Ψ^{iso-v}_{Res} streamfunctions.

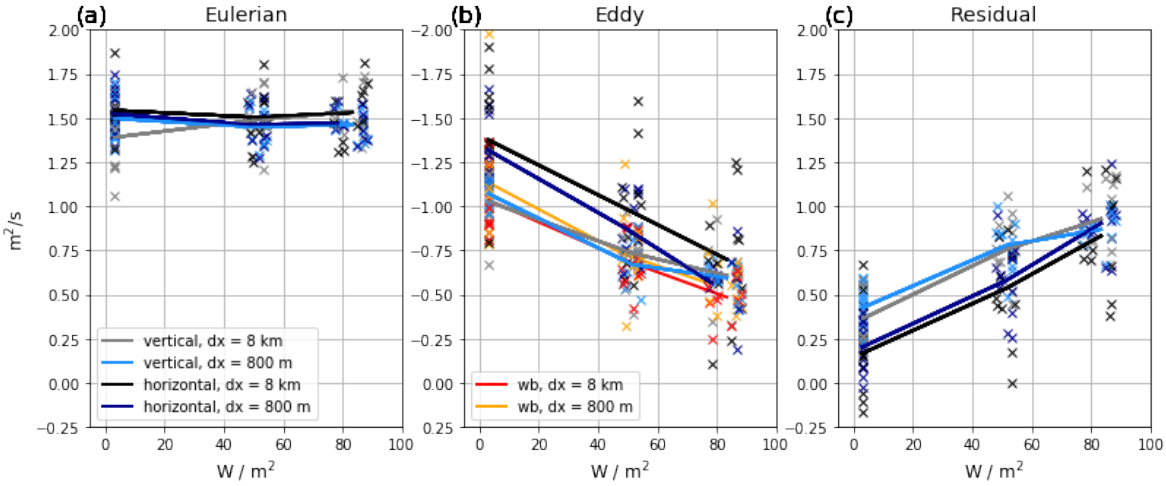

928 FIG. 10. Strength of Eulerian (a), eddy (b) and residual (c) streamfunction under varying heat flux forcing in 70
929 m depth at 64 km offshore (black cross in Fig. 7b, 8 and 9). Streamfunction estimates based on TEM theory (red,
930 orange; formulation 1), isopycnal integration of horizontal (black, dark blue; formulation 2) and vertical (gray,
931 light blue; formulation 3) velocities are shown for meso- and submesoscale horizontal resolution respectively.
932 Details on the calculation are in section 2c. Values found for each run of the ensembles are represented with a
933 cross. Solid lines connect the mean ensemble values found for the three different air-sea heat flux choices.

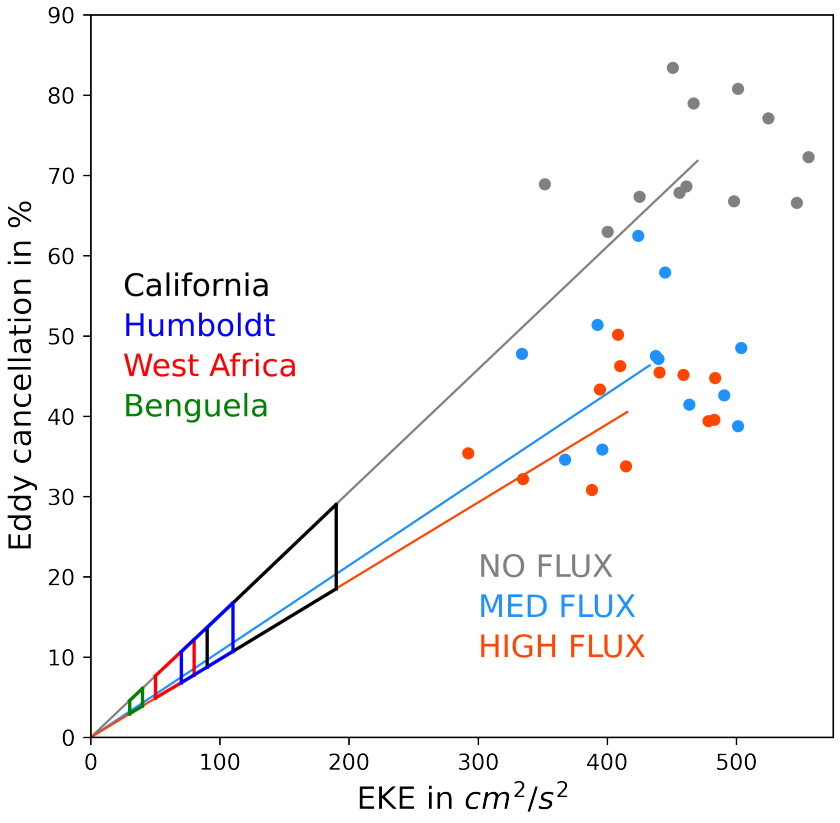

FIG. 11. Simulated eddy kinetic energy (EKE, in cm^2/s^2) vs. eddy cancellation (in %) from submesoscale simulations. The EKE values colored dots are derived from geostrophic velocity estimates of spatially filtered (rectangular centered 24 km running mean both in x and y direction) sea surface height anomalies of the dx = 800 m simulations (orange = HF, blue = MF and gray = NF case). The diagonal lines represent the best fit through the 12 ensembles of the different heat flux cases (same colorcode). The eddy cancellation in % for each individual ensemble run is estimated via $(\Psi^{iso-v}_{Mean} - \Psi^{iso-v}_{Res})/\Psi^{iso-v}_{Mean} * 100$. To put our idealized simulations in perspective, we also show satellite derived EKE ranges for different EBUS regions as solid boxes using EKE values provided by (Gruber et al. 2011) in their Figure S4 for California (26 - 32°N, black), Humboldt (12 - 18°S, blue), West Africa (12 - 18°N, red) and Benguela (12 - 18°S), green). Note that satellite derived EKE values taken from (Gruber et al. 2011) represent long term averages (1995-2003) wheres the short integration time of the idealized setting (40 days) only allows EKE estimates relative to alongshore mean SSH. Note that also higher or lower eddy cancellation can be expected in the different systems as we don't cover the full buoyancy forcing space observed in the real EBUS as show in Fig. 2b, c.